



Combining the advantages of GBT and shell finite elements: linear/non-linear analyses and modal decomposition

David Manta¹, Rodrigo Gonçalves², Dinar Camotim³

Abstract

This paper extends previous work by the authors, intended to contribute towards a more efficient modelling of thin-walled members and frames, by combining the advantages of Generalized Beam Theory (GBT) — mechanical clarity stemming from the modal decomposition of the solution — and conventional shell finite elements — versatility and reduced computational effort in non-linear problems. Two approaches are explored: (i) combining, in the same model, GBT-based beam and shell finite elements, and (ii) recovering the GBT deformation mode participations through post-processing shell finite element analysis results. The first approach, already presented by the authors (Manta et al. 2020, 2021a-c) for the geometrically linear and bifurcation cases, is now extended to large displacement elastic and elastoplastic analyses, using a geometrically exact beam finite element. In this approach, beam elements are used in the elastic and prismatic zones, while shell elements are employed in the remaining model. The second approach is useful when GBT-based beam elements cannot be used or are not computationally competitive and, since its implementation in standard finite element programs (such as commercial software packages) is relatively straightforward, it has a great potential of application in structural design, enabling the reinterpretation of shell finite element results in the light of GBT.

1. Introduction

It is now well established that the use of Generalized Beam Theory (GBT) to analyze thin-walled members and systems undergoing cross-section deformation (i) leads to very accurate solutions with a small computational cost in a wide range of structural analyses and (ii) provides in-depth insight into the mechanics of the problem under consideration, through the modal decomposition of the solution, stemming from the fact that the beam kinematic description is based on a set of hierarchical and structurally meaningful “cross-section deformation modes”. GBT was originally established by Schardt (1966, 1989, see <http://vtb.info>) and has been continuously improved by several researchers (*e.g.*, Nedelcu 2010, de Miranda et al. 2015, Cai & Moen 2016, Duan & Zhao 2019, Muresan et al. 2019, Camotim et al. 2010a-c, 2022, see also <http://www.civil.ist.utl.pt/gbt>).

¹ PhD Student, CERIS and Universidade Nova de Lisboa, Portugal <d.manta@campus.fct.unl.pt> >

² Associate Professor, CERIS and Universidade Nova de Lisboa, Portugal <rodrigo.goncalves@fct.unl.pt> >

³ Full Professor, CERIS, Instituto Superior Técnico, Universidade de Lisboa, Portugal <dcamotim@civil.ist.utl.pt>

The accuracy and computational efficiency of GBT is remarkable in geometrically linear (static or dynamic) and linear stability (bifurcation) analyses of members or frames constituted by prismatic bars. However, GBT (i) cannot be applied in systems with complex geometries (*e.g.*, complex joint configurations, tapered segments) and (ii) is not computationally competitive, with respect to shell finite element models, in physically non-linear problems, since many deformation modes (and hence many DOFs) are needed to obtain accurate results, which requires evaluating very large and dense element stiffness matrices at each iteration (Gonçalves & Camotim 2017). For this reason, some strategies involving stress or stress-resultant constraints have been devised (Gonçalves & Camotim 2004, 2011, 2012; Henriques et al., 2015, 2016). However, it is generally more efficient to combine shell and GBT-based finite elements in a single model (Manta et al. 2020, 2021a-c). In this approach, each element type is employed where it is most effective: (i) shell elements in the plastic and/or geometrically complex zones (tapered segments, holes, joints, etc.) and (ii) GBT-based elements in prismatic and elastic zones. This makes it possible to include only a small number of deformation modes in the GBT elements, without sacrificing accuracy, as the zones whose correct GBT modelling would require many deformation modes are instead (and more efficiently) handled using shell elements. This approach was shown to be capable of handling complex geometries and phenomena with great computational efficiency (with respect to full shell models) while preserving the advantages of the GBT modal decomposition features, in a wide range of analyses: (i) geometrically linear static (elastic and elastoplastic), (ii) geometrically linear dynamic, (iii) vibration (including geometrically non-linear effects) and (iv) linear stability (bifurcation) analyses. It should be mentioned that the combination of GBT-based and shell elements to model connections has also been proposed by Bianco et al. (2019), Hansen & Jönsson (2019) and Hansen et al. (2022), although only linear elastic analyses of systems having prismatic bars were dealt with.

The simplifying assumptions adopted in GBT hinder its application in the moderate-to-large displacement range: (i) Kirchhoff's assumption only holds for small displacements and (ii) the deformation modes describe linearized (not finite) rotations. For instance, as shown in Fig. 1, a cross-section rigid-body torsion cannot be described by the torsion deformation mode alone, as it causes a cross-section in-plane enlargement and cannot exceed 90° , making it indispensable to include transverse extension modes to compensate for this effect (hence such transverse extension modes appear in the solution, even if they are not associated to the structural behavior). This leads to the need to include many deformation modes in the analysis, leading to an increase of the computational cost. To overcome this problem, beam finite elements that rely on rotation tensors and incorporate GBT deformation modes have been proposed (Gonçalves et al. 2010, 2011, Peres et al. 2021). Naturally, such elements become progressively expensive as the number of deformation modes is increased (as required in physically non-linear problems and/or when severe cross-section deformation occurs) and, moreover, still cannot handle complex geometries.

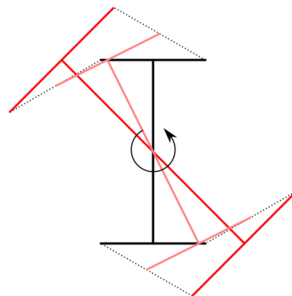


Figure 1: Cross-section in-plane enlargement due to the GBT torsional mode (an I section is shown)

When beam finite elements including cross-section deformation cannot be employed or its use is not computationally competitive, shell elements must be used. However, a GBT mode decomposition of the solution can still be achieved through post-processing. This approach was first proposed by Nedelcu (2012), for the identification of buckling (bifurcation) modes of members with open cross-section. Henriques et al. (2016) devised a similar approach to handle discrete wall thickness longitudinal variations, using non-orthogonal GBT deformation modes in the analysis and recovering *a posteriori* the participation of the orthogonal modes, by means of a standard change of basis operation. This procedure was extended by Gonçalves & Camotim (2017) using a nodal DOF-based GBT approach, which can handle efficiently perforations and plasticity. More recently, Cai (2019) applied a post-processing procedure to obtain the GBT mode decomposition from shell model bifurcation analyses. At each cross-section, the GBT mode amplitudes are calculated using a least square fit of the shell model cross-section in-plane displacements. The participation of the axial extension mode is recovered by calculating the average cross-section warping. Finally, the mode amplitude functions are calculated by interpolating their values at four consecutive cross-sections, using Hermite cubic polynomials. Since this method is based exclusively on cross-section in-plane displacements, it cannot be applied to problems where membrane shear strains are relevant. Furthermore, only the so-called conventional deformation modes were considered, meaning that, beside the shear modes, the transverse extension modes were discarded.

This paper extends previous work along two directions, combining the advantages of GBT and standard shell finite elements:

- (i) Recovering GBT mode participations through post-processing shell element model results. This approach is herein extended to all cross-section deformation mode families, several analysis types — bifurcation, vibration, first-order/large displacement elastic and elastoplastic — and members with complex geometries (*e.g.*, tapered or curved segments, joints). It is also shown that it can be applied to finite strip results. In the large displacement range, to circumvent the fact that the GBT deformation modes are not suitable to describe finite rotations, the concept of “cross-section strain modes” is introduced.
- (ii) Combining beam and shell elements in the same model. This concept is extended to the large displacement elastic and elastoplastic cases. As already explained, in this displacement range GBT-based finite elements cannot be employed and thus the geometrically exact beam element proposed by Peres et al. (2021) is used instead, which can incorporate GBT deformation modes. This element handles moderate cross-section deformation and is thus employed to detect the zones where significant local/distortional buckling and/or plasticity occur. Subsequently, these zones are re-meshed using shell elements (much more efficient in such zones).

Throughout the paper, several illustrative numerical examples are presented and discussed, to validate and show the capabilities and potential of the proposed approaches.

Concerning the notation, scalars are represented by *italic* letters and vectors/matrices by ***bold italic*** letters. The identity matrix is represented by **I** and null matrices/vectors by **0**. Furthermore, a derivative is represented by a subscript comma (*e.g.*, $f_{,a} = \partial f / \partial a$), a virtual variation is denoted by δ and an incremental/iterative variation by Δ .

2. Brief overview of the adopted shell and beam finite elements

This section provides a brief overview of the main features of the shell and beam finite elements employed. In all cases the equilibrium equations are obtained using virtual work, written in terms of Green-Lagrange strains and second Piola-Kirchhoff stresses, which ensures that the beam finite element captures Wagner effects. Small strain J_2 (Mises) plasticity with associative flow rule and no hardening is implemented. For elastic strains/stresses, a standard St. Venant-Kirchhoff material law is adopted. At each iteration, the plastic stresses are updated using the backward Euler return scheme (Simo & Taylor 1985). The finite element procedure and post-processing calculations (such as the recovery of the GBT mode participation and the representation of deformed configurations, mode shapes and stress fields) were implemented in MATLAB (2010).

The shell element adopted is the well-known 4-node Reissner-Mindlin Mixed Interpolation of Tensorial Components (MITC-4) element shown in Fig. 2(a) (Bathe 1996, Bathe & Dvorkin 1985), even if any other shell element could have been used. This element can handle large displacements and relies on linear interpolation. Shear locking is mitigated by re-interpolating the covariant through-thickness shear strains, in the convected system (r, s, t) , from the corresponding values at the so-called “tying points”, which in MITC-4 lie at the middle of each mid-surface edge. The element is mapped through

$$\mathbf{x} = \bar{\mathbf{x}} + \frac{th}{2} \mathbf{v}_n, \quad (1)$$

where vector $\bar{\mathbf{x}}$ maps the mid-surface, h is the shell thickness and \mathbf{v}_n is the thickness director vector. The mid-surface vector $\bar{\mathbf{x}}$ is obtained by interpolating the nodal displacements, whereas \mathbf{v}_n is interpolated from its nodal values. After each iteration, the nodal vectors \mathbf{v}_n are updated using a rotation tensor which is parametrized with the (iterative) rotation vector. Since the shell drill DOF is not considered, only two components of the rotation vector are required and thus the element has 5 DOFs per node (3 translations and 2 rotations), leading to a total of 20 DOFs. The integration of the element tangent stiffness, mass matrix and internal force vector is carried out

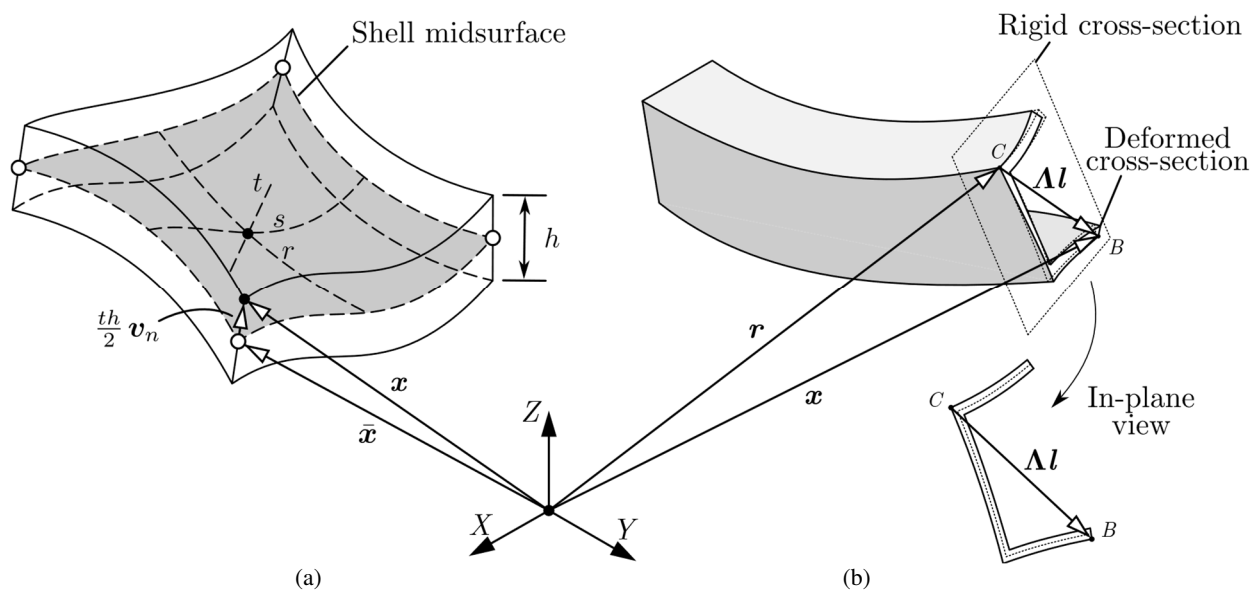


Figure 2: (a) MITC-4 shell element and (b) geometrically exact beam element

with Gauss quadrature, using a mid-surface grid with 2×2 points and 3 or 5 points in the thickness direction for the elastic and elastoplastic analyses, respectively.

The beam element employed was proposed by Peres et al. (2021) and is termed “geometrically exact” in the sense that no geometric simplifications are introduced besides the assumed kinematics, a concept pioneered by Reissner (1972) and Simo (1985). The element can handle naturally curved thin-walled members and arbitrary cross-section deformation complying with Kirchhoff’s thin-plate assumption, but the shell-like bending strains are assumed small. As shown in Fig. 2(b), the position of an arbitrary point B , is given by

$$\mathbf{x} = \mathbf{r} + \widehat{\Lambda}\Lambda_0\mathbf{l}, \quad (2)$$

where \mathbf{r} is the position vector of the cross-section arbitrary center C , Λ_0 is the rotation tensor to the initial configuration, $\widehat{\Lambda}$ is the rotation tensor from the initial to the current configuration, which is parametrized using the 3D rotation vector $\widehat{\boldsymbol{\theta}}$, and vector \mathbf{l} maps the position of each cross-section point with respect to C through

$$\mathbf{l} = \mathbf{l}_0 + \mathbf{R} \sum_{i=1}^D \chi_i \phi_i, \quad (3)$$

where \mathbf{l}_0 is the counterpart of \mathbf{l} for the initial configuration, \mathbf{R} is a rotation tensor that changes the coordinate system such that the deformation modes can be written in a wall local frame, χ_i is the displacement vector pertaining to the GBT deformation mode i and ϕ_i is its corresponding amplitude function along the beam axis, and D is the number of deformation modes included in the analysis. The finite element interpolates the independent kinematic parameters (three translations, three rotations and D parameters) using Hermite cubic polynomials, leading to a two-node element with $2(6+D)$ DOFs per node. The wall mid-surface integration is carried out with a 3×3 Gauss point grid, which corresponds to reduced integration, to mitigate shear and membrane locking. Along the thickness, analytical integration is possible since the shell-like bending strains are assumed small.

3. The GBT kinematic description and the deformation modes

The GBT kinematic description is based on wall local axes (x, y, z) , defining the member axis, wall mid-line and thickness directions, respectively (see Fig. 3). Using Kirchhoff’s thin plate assumption for small displacements, the displacement vector for each wall is expressed as

$$\mathbf{U} = \begin{bmatrix} U_x \\ U_y \\ U_z \end{bmatrix} = \begin{bmatrix} (\bar{\mathbf{u}} - z\bar{\mathbf{w}})^T \boldsymbol{\phi}_{,x} \\ (\bar{\mathbf{v}} - z\bar{\mathbf{w}}_{,y})^T \boldsymbol{\phi} \\ \bar{\mathbf{w}}^T \boldsymbol{\phi} \end{bmatrix}, \quad (4)$$

where $\bar{\mathbf{u}}(y)$, $\bar{\mathbf{v}}(y)$, $\bar{\mathbf{w}}(y)$ are column vectors containing the displacement components of the GBT cross-section deformation modes along x , y and z , respectively, and $\boldsymbol{\phi}(x)$ is a column vector collecting the corresponding amplitude functions, which constitute the problem unknowns.

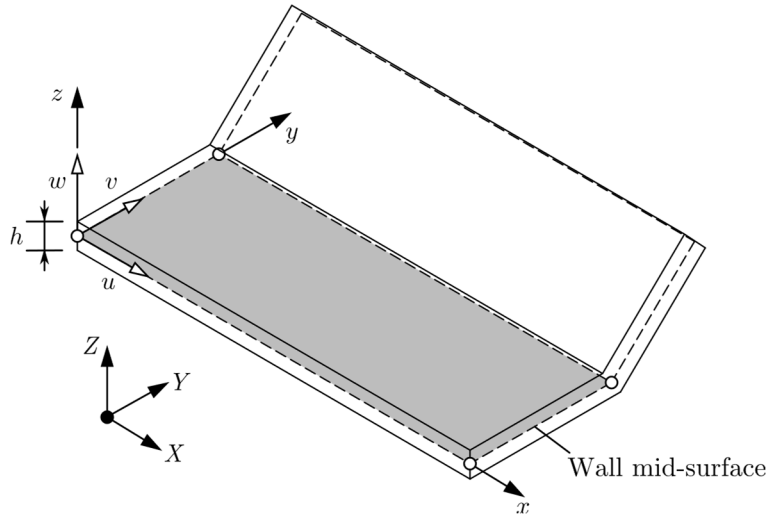


Figure 3: GBT wall local axes and displacement components

The deformation modes are obtained from the so-called “GBT cross-section analysis” procedure, which is described in detail by Gonçalves et al. (2014) and Bebiano et al. (2015). This procedure is implemented in the GBTUL program (Bebiano et al. 2018), which is freely available at www.civil.ist.utl.pt/gbt. In this work, the GBT deformation modes are always calculated using GBTUL and it is worth recalling that they are obtained by first discretizing the cross-section mid-line using mandatory *natural nodes*, located at wall intersections and free ends, and user-defined *intermediate nodes*, located between natural nodes with the purpose of refining the displacement field. Three DOFs are assigned to each node (the cross-section in-plane rotations are condensed out) and are interpolated along the mid-line as explained by Bebiano et al. (2018). The deformation modes are obtained through several change of basis operations, leading to the following mode sets:

- (i) *Conventional modes*, comprising “rigid-body” (axial extension, bending about central principal axes and torsion about the shear center), distortional and local-plate modes. These modes satisfy Vlasov’s null membrane shear strain assumption (except the torsion mode for sections with cells) and the null membrane transverse (along y) strain assumption. Due to these assumptions, the conventional modes generally suffice to obtain very accurate results.
- (ii) *Shear modes*, which relax Vlasov’s assumption and are subdivided into (I) cell shear flow modes, only appearing in sections with cells (although the torsion mode belongs to this set in such sections, in GBTUL it is included in the conventional mode set), (II) the warping functions of the bending, torsion (in open sections) and distortional conventional modes, and (III) additional warping functions that complete the shear mode space.
- (iii) *Transverse extension modes*, which do not enforce the previous two assumptions and complete the deformation mode space pertaining to the adopted cross-section discretization.

In this work, the GBT deformation modes are always calculated using the GBTUL engine, which means that the GUI is bypassed and fast computation times are ensured.

4. Recovery of GBT modal decomposition

4.1 Geometrically linear and bifurcation analyses

First, geometrically linear and bifurcation (linear stability) analyses are addressed, in which case small-to-moderate displacements are assumed and thus the decomposition of the shell or finite strip displacement field in terms of GBT deformation modes leads to structural insight. The

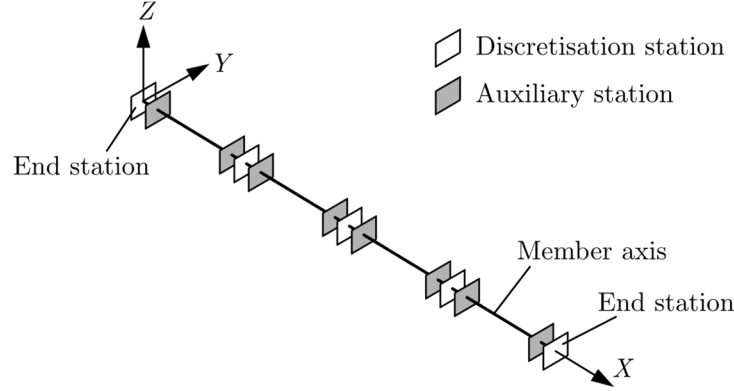


Figure 4: Subdivision of the member axis into stations

proposed procedure is performed at a given number of cross-sections, termed *discretization stations* and *auxiliary stations*, as shown in Fig. 4. The procedure is identical for both station types, but a distinction is made since the auxiliary stations are solely used for calculating the amplitude function derivatives — such derivatives are more accurate if the auxiliary stations are close to the discretization stations (naturally, they can also coincide).

Although the mode amplitude values between stations can be obtained by interpolating the results at each station (Cai 2019), this is not advisable in the presence of localized effects (*e.g.*, due to concentrated forces or plastic strains), since a fine station mesh would be required, resulting in an increase of the computational cost. Instead, it is advocated that the mode amplitudes should be calculated for a somewhat coarse mesh of discretization stations, since the main advantage of the recovery procedure is to provide an in-depth insight on the mechanics underlying the problem, rather than to capture accurately the mode amplitude functions (which is obviously possible with a refined mesh). The proposed procedure involves the following steps:

- (i) A set of discretization stations is defined along the beam axis, in the finite strip (FS) or shell finite element (SFE) model.
- (ii) The GBT deformation modes are calculated for each cross-section, using GBTUL and a user-defined cross-section discretization which does not require many intermediate nodes, since this simply introduces higher-order modes that, in general, have small participations and little relevance to characterize the mechanics of the problem at hand.
- (iii) At each discretization station, a set of appropriate FS/SFE wall mid-line nodes is selected and their displacements (not rotations) along the GBT local axes are collected in vectors $\bar{\mathbf{U}}_x$, $\bar{\mathbf{U}}_y$ and $\bar{\mathbf{U}}_z$. In the illustrative examples presented next, these nodes coincide with the GBT cross-section discretization, but nothing prevents the selection of additional nodes. In the following, it is assumed that the number of deformation modes does not exceed the number of selected FS/SFE DOFs (the sum of the dimensions of $\bar{\mathbf{U}}_x$, $\bar{\mathbf{U}}_y$ and $\bar{\mathbf{U}}_z$).
- (iv) For the modes involving cross-section in-plane displacements (*i.e.*, the conventional modes excluding axial extension, the type I shear modes and the transverse extension modes), the relation between the FS/SFE DOFs and the GBT modes at a station can be written as

$$\begin{bmatrix} \bar{\mathbf{U}}_y \\ \bar{\mathbf{U}}_z \end{bmatrix} = \mathbf{T}_{yz} \boldsymbol{\phi}, \quad \mathbf{T}_{yz} = \begin{bmatrix} \mathbf{T}_y \\ \mathbf{T}_z \end{bmatrix}, \quad (5)$$

where element ij of matrix \mathbf{T}_k contains the displacement along axis k of mode j at DOF i and $\boldsymbol{\phi}$ is a column vector that contains the unknowns (mode amplitude function values at the station under consideration). The system is subsequently solved for $\boldsymbol{\phi}$. If the number of selected FS/SFE DOFs equals the number of GBT deformation modes, \mathbf{T}_{yz} is square and invertible, otherwise the system is over-determined and is solved with the method of least squares.

- (v) Finally, the amplitudes of the axial extension and type II/III shear modes, which only involve warping, are recovered. Note, from Eq. (4), that the warping displacements U_x depend on $\phi_{,x}$ instead of $\boldsymbol{\phi}$. For these deformation modes one first solves

$$\bar{\mathbf{U}}_x = \mathbf{T}_x \mathbf{a}_x, \quad (6)$$

where element ij of matrix \mathbf{T}_x contains the warping displacement of mode j at DOF i and vector \mathbf{a}_x collects the corresponding amplitudes, which are once more calculated by inverting \mathbf{T}_x or using the least squares method. The amplitudes of the axial extension and type III shear modes are given by $\phi_{k,x} = (\mathbf{a}_{,x})_k$. However, recall that the warping functions of the type II shear modes coincide with those of the bending, torsion (for open sections) and distortional conventional modes. For this reason, for each type II shear mode k , the derivative of the amplitude function of the corresponding conventional mode j must be calculated (as explained next) and the amplitude of the shear mode is obtained from the relation

$$\phi_{k,x} = (\mathbf{a}_{,x})_k - \phi_{j,x}. \quad (7)$$

To calculate $\phi_{j,x}$, the finite difference method is used, adopting central differences for inner stations and forward/backward differences for the member ends. To minimize the error associated with the finite difference scheme when a coarse discretization station mesh is used, auxiliary stations adjacent to the target station can be defined, as shown in Fig. 4.

4.2 Validation and illustration of the mode amplitude recovery procedure

First, three validation examples are presented. The first one concerns the linear stability analysis of the simply supported lipped channel columns shown in Fig. 5(a). The signature curve is calculated using (i) the semi-analytical Finite Strip Method (FSM), which relies on single half-wave sinusoidal longitudinal functions and was implemented in an in-house program, and, for validation purposes, (ii) the semi-analytical method available in GBTUL, which also uses the above functions, including only the conventional deformation modes (which suffices in this standard benchmark case). The cross-section discretization employed in both analyses is also shown in the figure, leading to 12 GBT conventional deformation modes and 40 FSM DOFs. The proposed mode amplitude recovery procedure is applied to the FSM results and, since the longitudinal functions are known, a single station at mid-span suffices. The results are presented in Fig. 5(b). The top graph displays the signature curve obtained with the FSM and GBTUL, showing a perfect match (as expected). Attention should be drawn to the bottom mode participation diagram (calculated using a linear strain energy criterion), which shows that there is an excellent agreement between the results obtained with GBTUL and the proposed procedure, *i.e.*, that the proposed procedure reproduces exactly the GBTUL solution even though it is based on FSM results.

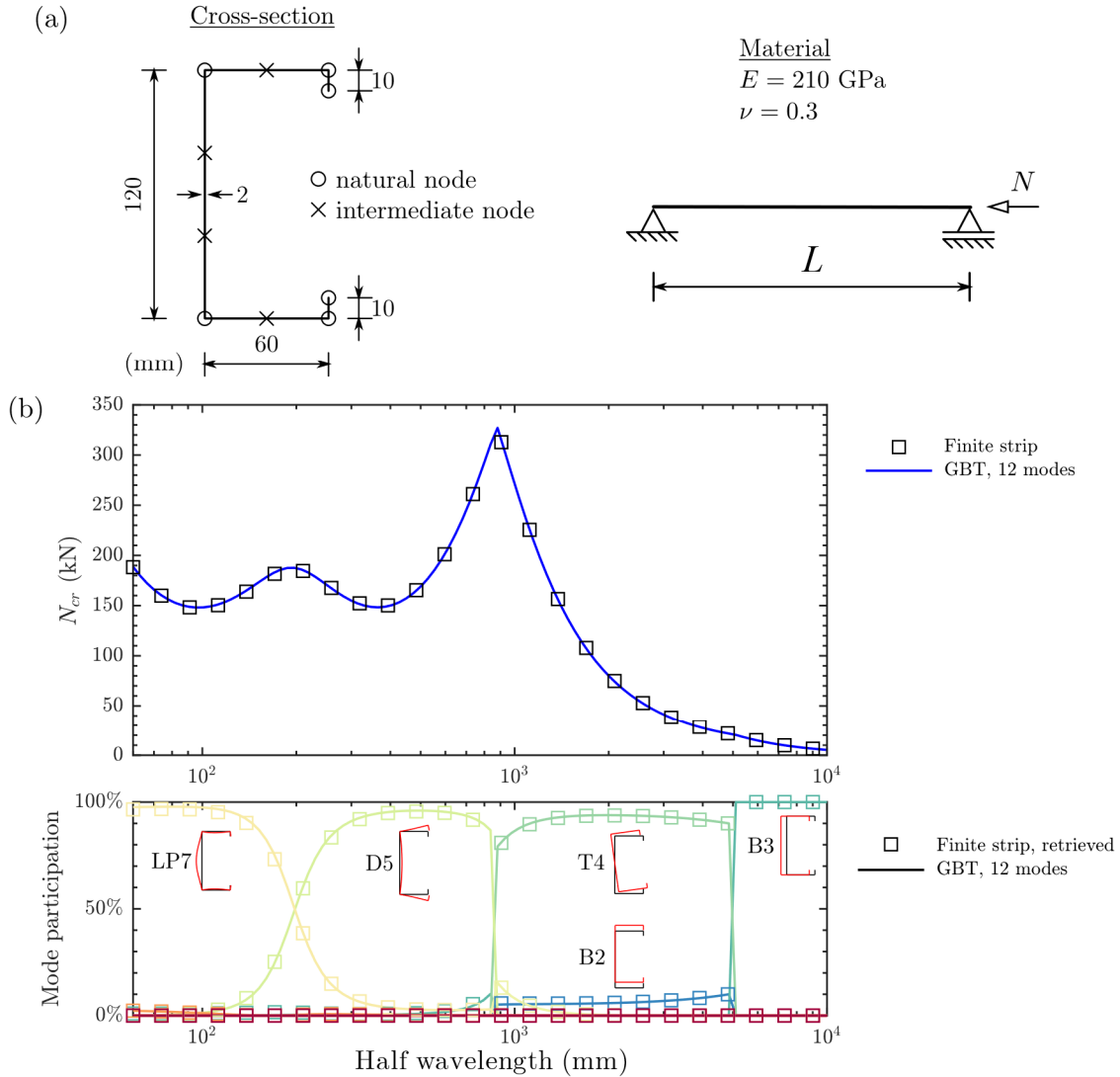


Figure 5: Elastic buckling analysis of simply supported lipped channel columns: (a) geometry, loading, cross-section discretization and material parameters, and (b) signature curve and GBT mode participation diagram

The second validation example consists of the first-order analysis of the lipped channel cantilever shown in Fig. 6(a), carried out using shell and GBT-based finite element models. The mode amplitudes are recovered from the shell model results and compared with those of the genuine GBT analysis, again performed in GBTUL. The GBT cross-section discretization adopted leads to 45 deformation modes: 1-17 conventional, 18-31 shear and 32-45 transverse extension. Three models are considered: (i) a refined shell model with 1040 elements (Fig. 6(b)) and (ii) two GBT-based finite element models, using 10 equal length elements and including either the 17 conventional modes or all 45 modes. Fig. 6(b) displays the deformed configurations and the displacement of the load application point provided by all models, although the GBT deformed configuration with all modes is not shown, since there is no visible difference with respect to that obtained with 17 modes. Even though the deformed configurations are in excellent agreement, the table reveals that the GBT solution with 17 modes leads to a 7.7% displacement difference, which drops to just 0.40% when all 45 modes are considered — this shows that, although barely visible,

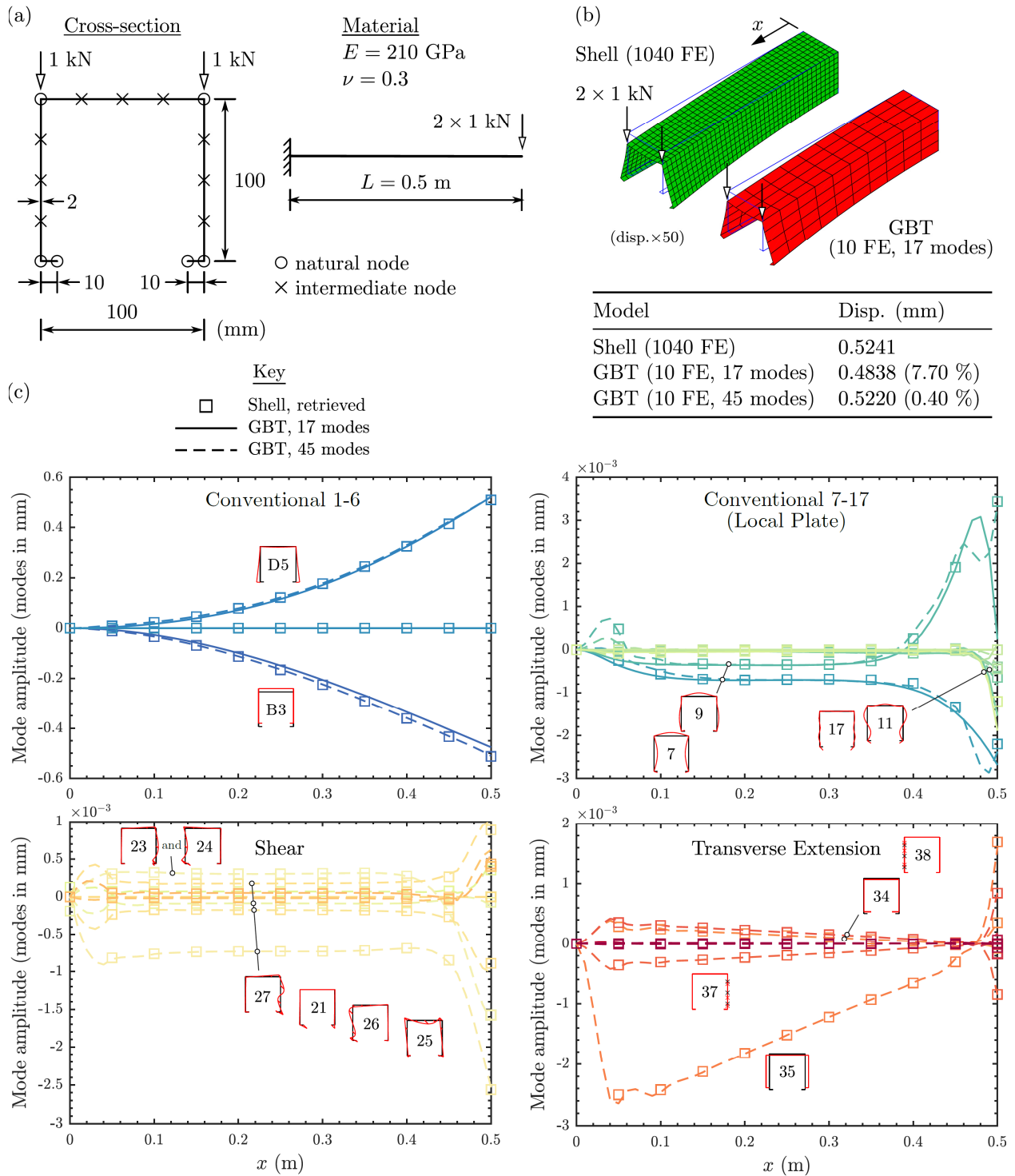


Figure 6: First-order analysis of a lipped channel cantilever: (a) geometry, loading, cross-section discretization and material parameters, (b) deformed configurations and displacement of the loaded point, (c) GBT mode amplitudes

the shear and transverse extension modes are essential to reach accurate results in this problem (precisely the reason for its selection). Fig. 6(c) displays the mode amplitude diagrams (i) recovered from the shell model, using 11 equally spaced stations, and (ii) obtained with both GBT

models. Although this problem is clearly governed by minor-axis bending (B3) and symmetric distortion (D5), it is shown that, despite their small amplitudes, the inclusion of the shear and transverse extension modes is essential to obtain accurate results — note that the mode amplitude functions with 17 or 45 modes differ in the two top diagrams, particularly for the local-plate modes. However, the most important conclusions drawn from these diagrams are that (i) the recovered mode amplitudes are in excellent agreement with the full 45 mode GBT model solution and (ii) the proposed procedure can retrieve accurately the amplitudes of all deformation mode families.

The final validation example concerns the vibration analysis of the simply supported twin-cell beams shown in Fig. 7(a). The cross-section discretization leads to 90 deformation modes: 29 conventional, 1 distortional cell shear flow, 31-59 additional shear and 60-90 transverse extension. Three models are considered: (i) refined shell models (see Fig. 7(b)), taking advantage of the problem symmetry, and two GBT semi-analytical solutions (obtained with GBTUL, using sinusoidal amplitude functions) including either (ii) the conventional and distortional cell shear flow modes (30 modes) or (iii) all 90 modes. Fig. 7(b) displays the shell model vibration modes for selected lengths, whereas Fig. 7(c) shows the fundamental frequencies, as a function of the span L , together with the corresponding mode participation diagrams (again based on a linear strain energy criterion). The GBT mode participations recovered from the shell results were obtained using 11 equally spaced stations. It is concluded that there are essentially three types of vibration modes: (i) local-plate (mode 7) for $L < 900$ mm, (ii) distortional (mode 6) for $900 < L < 1300$ mm and (iii) minor-axis bending (B3) for $L > 1300$ mm. The top graph makes it possible to conclude that there are minute differences between the three models, but the most relevant conclusions for the present paper concern the bottom graph, where it is once more confirmed that the results of the proposed recovery procedure once more virtually match those of the genuine GBT refined model. Note that, with respect to the coarse GBT model (30 modes), the participations of the distortional mode 6 (for intermediate L) and the bending mode 3 (for large L) decrease, as several higher-order modes are triggered, most notably the transverse extension mode 64 (for $L > 1300$ mm).

Next, three examples are presented to illustrate the capabilities of the proposed recovering procedure in complex problems, for which GBT cannot be applied or is not efficient from a computational point of view.

First, a linear analysis of the tapered lipped channel cantilever shown in Fig. 8(a) is carried out. The cross-section discretization adopted leads to 17 conventional modes (1-4 rigid body, 5-6 distortional and 7-17 local-plate) which are the only ones included in the analysis, since the remaining modes have negligible amplitudes. The shell model employed is shown in Fig. 8(b). For the application of the proposed procedure, the shell model is discretized using either 11 or 51 equally spaced stations (10 or 50 divisions, respectively). It should be noted that GBT cannot be used to solve this example and thus the proposed procedure provides the only way to obtain the modal decomposition of the solution. Since the beam is tapered, each station has a different set of deformation modes, but the computational cost involved is quite small, since the GBTUL engine is employed. Interestingly, the major axis is vertical at the free end and horizontal at the support. For this reason, to keep the mode numbering consistent, the bending modes are switched so that the B3 mode always corresponds to bending about the horizontal axis. Fig. 8(b) shows the deformed configuration obtained with the shell model, evidencing bending and symmetric

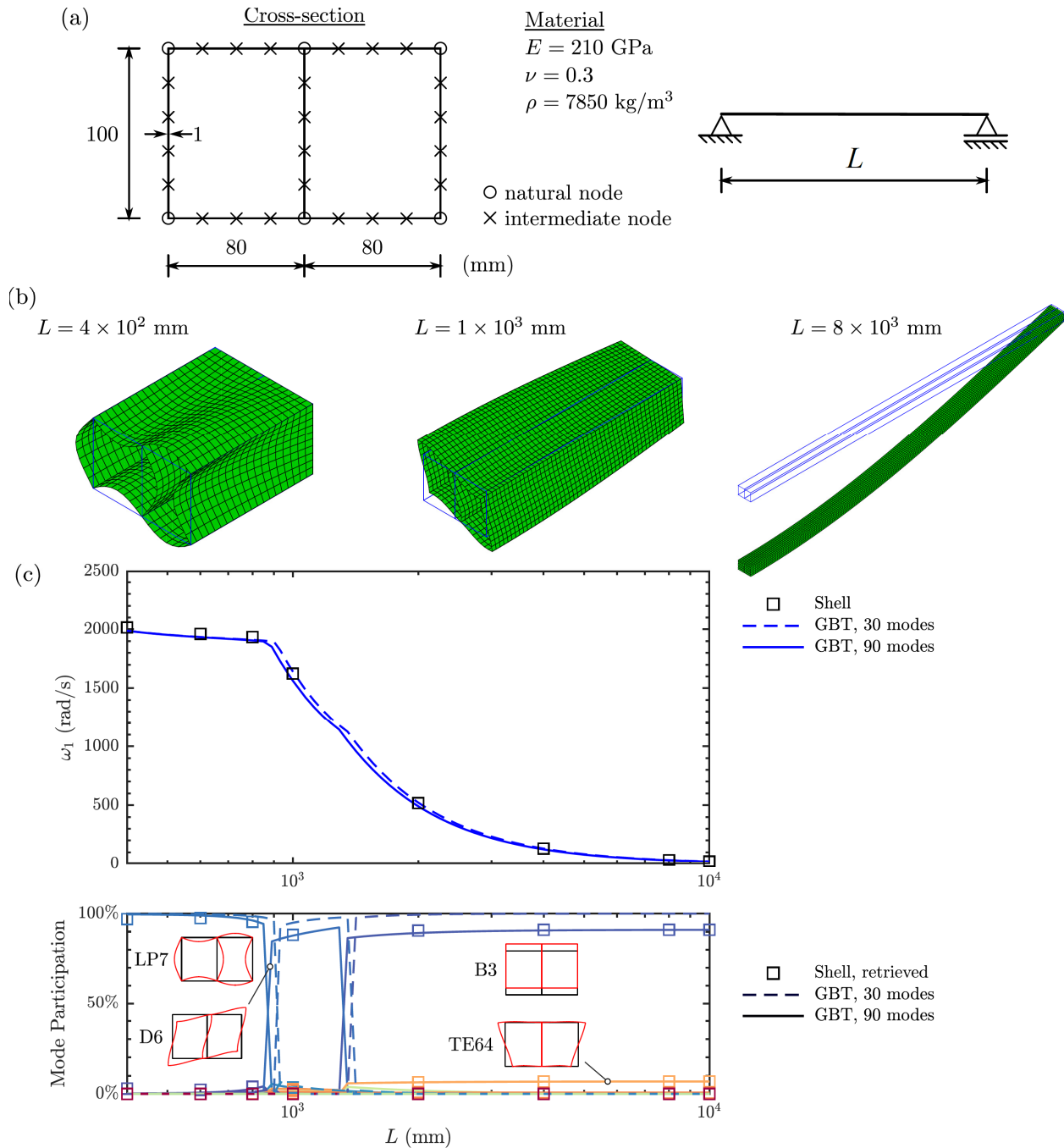


Figure 7: Vibration analysis of a simply supported twin-cell beam: (a) geometry, cross-section discretization and material parameters, (b) selected vibration mode shapes for one half of the beams, (c) fundamental frequencies as a function of the span L and GBT mode participation diagrams

distortion. Fig. 8(c) displays the amplitude functions of the most relevant rigid-body and distortional conventional modes along the beam axis and confirm the previous assertion: symmetric distortion (D5) and bending (B3) have dominant participations, even though axial extension (E1) is also present, due to the inclination of the line of centroids (it is not horizontal). It is also concluded that the amplitude functions obtained with 11 stations (10 subdivisions)

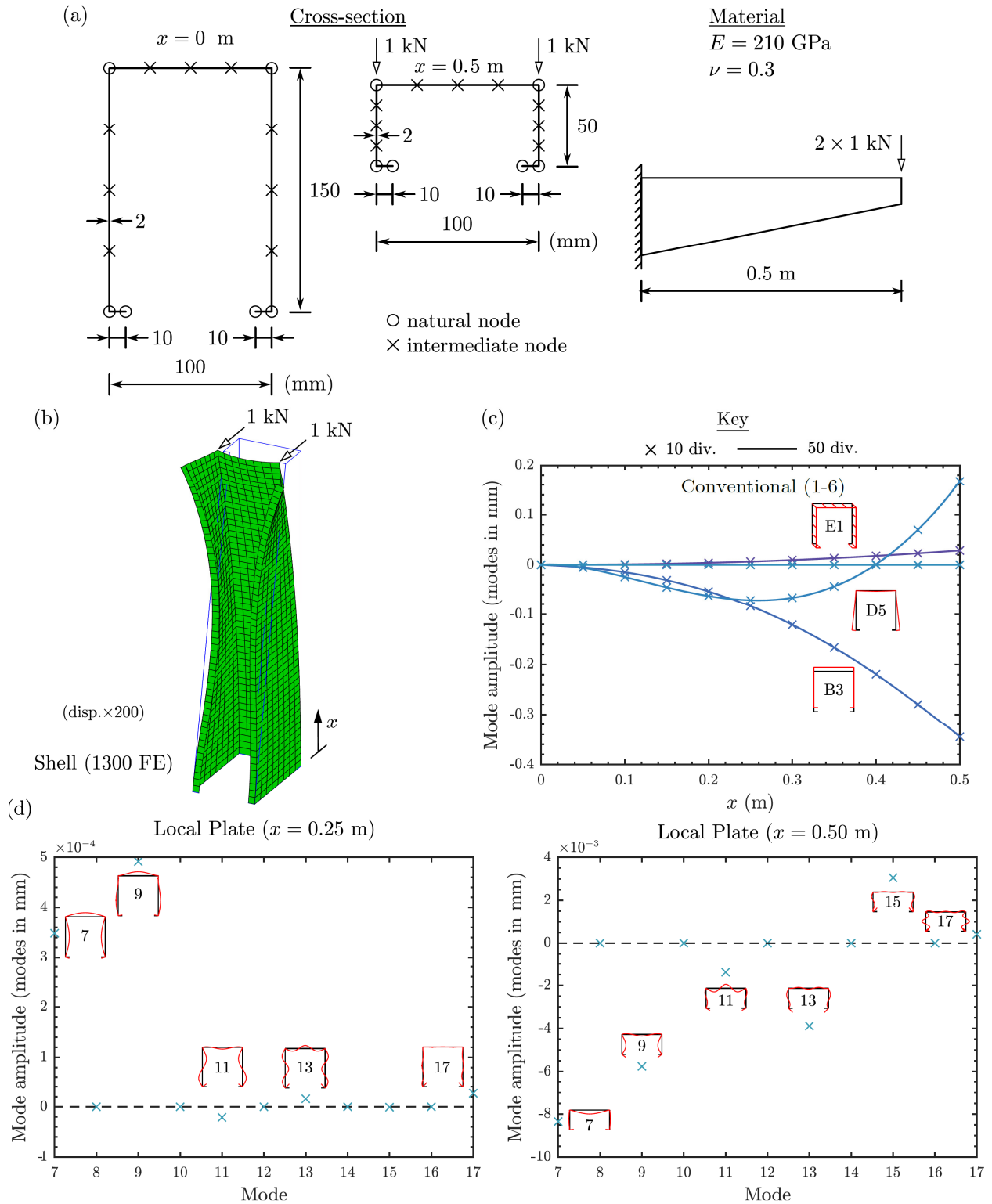


Figure 8: First-order analysis of a tapered lipped channel cantilever: (a) geometry, loading, cross-section discretization and material parameters, (b) shell model deformed configuration, (c) conventional mode amplitude functions and (d) local-plate mode amplitudes at mid-span ($x = 0.25$ m) and free end ($x = 0.5$ m)

virtually coincide with those obtained with 51 stations (50 subdivisions). Finally, Fig. 8(d) shows the local-plate mode amplitudes at mid-span (left graph) and at the free-end (right graph) — note that the number of stations is irrelevant, since no derivatives need to be computed. The corresponding amplitude functions are not shown because the deformation mode shapes vary quite significantly, which means that the mode amplitudes are more meaningful locally (at a given station). These graphs show that the local-plate modes have higher amplitudes at the free end than at mid-span, and that the modes relevant at both stations are practically the same. However, it should be noted that these mode amplitudes are several orders of magnitude below the conventional mode ones shown in Fig. 8(c).

The next example consists of the first-order analysis of an I-section cantilever with a straight and a 90° curved segments (Fig. 9(a)). The selected GBT cross-section discretization leads to 15 conventional modes (1-4 rigid body and 5-15 local-plate). The proposed procedure is applied by subdividing the straight/curved segments into 40/70 equally spaced segments (41/71 stations), respectively. In the curved segment, the global axes are rotated at each section, so that x is always

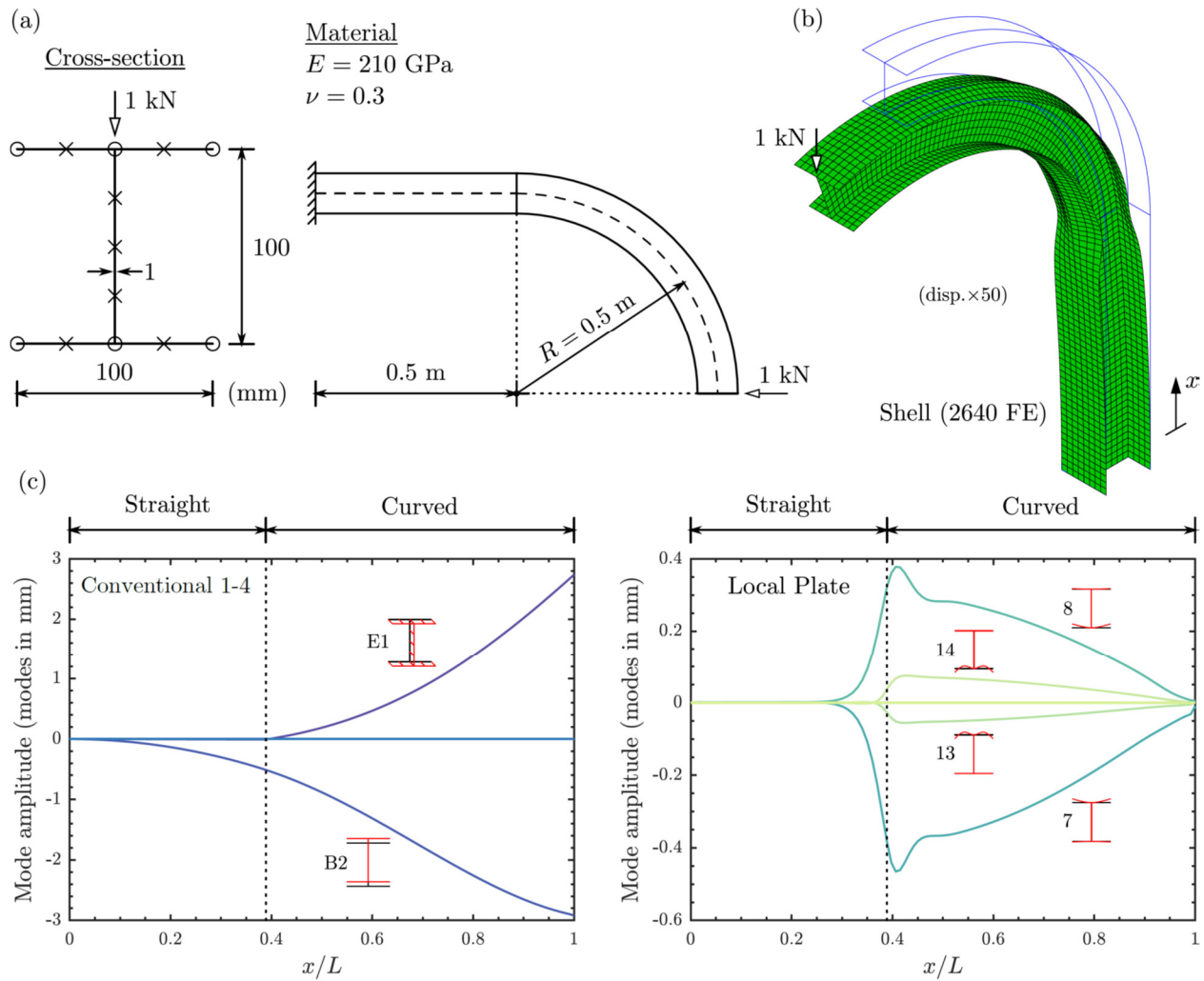


Figure 9: First-order analysis of an I-section cantilever with a curved segment: (a) geometry, loading, cross-section discretization and material parameters, (b) shell model deformed configuration and (c) mode amplitude functions

tangent to the member longitudinal axis. Fig. 9(b) shows the deformed configuration obtained with the shell model, being worth noting that significant flange curling occurs at the curved-straight boundary (both flanges bend towards the neutral axis). The mode amplitude diagrams in Fig. 9(c) reveal that (i) major-axis bending is naturally present throughout the beam, (ii) some axial extension appears in the curved part (bending in curved members causes axial displacements) and (iii) flange curling essentially involves modes 7 and 8 (the amplitudes of modes 13 and 14 are much smaller) and is maximum near the straight-curved boundary, with both flanges bending towards the neutral axis — note that the amplitude of mode 7 is negative, hence its configuration is inverted. Flange curling practically does not occur in the straight segment.

The last example concerns the elastoplastic simply supported hat section beam displayed in Fig. 10(a), which was originally analyzed by Gonçalves & Camotim (2011). In this case all GBT deformation modes are recovered (conventional 1-4 rigid-body, 5-6 distortional and 7-29 local-plate, shear 30-55 and transverse extension 56-81). In the shell model (Fig. 10(c)), two symmetry simplifications are adopted. The proposed procedure is applied with either 11 or 51 equally spaced stations (10/50 subdivisions). The graph in Fig. 10(b) provides the relation between the applied loads and their work-conjugate displacements, obtained with the shell model, evidencing a significant stiffness reduction after the onset of yielding. Fig. 10(c) displays several deformed configurations (the yellow elements have at least one yielded integration point), showing that significant distortion occurs throughout the beam and that the top flange develops a bulge at mid-span for the two highest displacement values. The diagrams in Fig. 10(d) plot the GBT mode amplitude functions corresponding to the first and last deformed configurations in Fig. 10(c), for both station discretization schemes. It is observed that, for both displacement values, minor-axis bending (B3) and symmetric distortion (D5) are the most relevant modes, for which both station discretizations yield identical results. Localized deformation occurs at mid-span (the previously mentioned top flange bulge), with significant participation from the local-plate modes and, to a lesser and more localized extent, also from a few shear and transverse extension modes. The coarse station discretization captures quite well the local-plate mode amplitudes, but only the refined one can accurately capture the shear mode amplitudes near mid-span. Finally, note that, due to the symmetry, the amplitudes of the asymmetric shear and transverse extension modes 36, 40 and 62 match their reflection counterparts (modes 37, 41 and 63), having opposite signs when the mode shapes are inverted (modes 41 and 63).

4.3 Large displacement elastic and elastoplastic analyses

As explained in Section 1, the GBT deformation modes are not suited for analyses involving large displacements. For this reason, the proposed mode recovery procedure does not rely on displacements but instead on Green-Lagrange strains, calculated from a large displacement shell finite element analysis, which are decomposed into GBT membrane/curvature *strain modes*. Since the Green-Lagrange strains are invariant under rigid-body motions and describe the deformation of elementary vectors defined at the initial configuration, a very clear physical interpretation of the results is ensured, leading to a straightforward identification of the most relevant deformation modes, while circumventing the lack of suitability of the GBT deformation modes. The individual strain components generated by each GBT deformation mode — the strain modes — define the basis onto which the shell model strains are projected. The fact that the strain modes are calculated using small strain theory is of particular relevance, since it establishes a physically clear basis

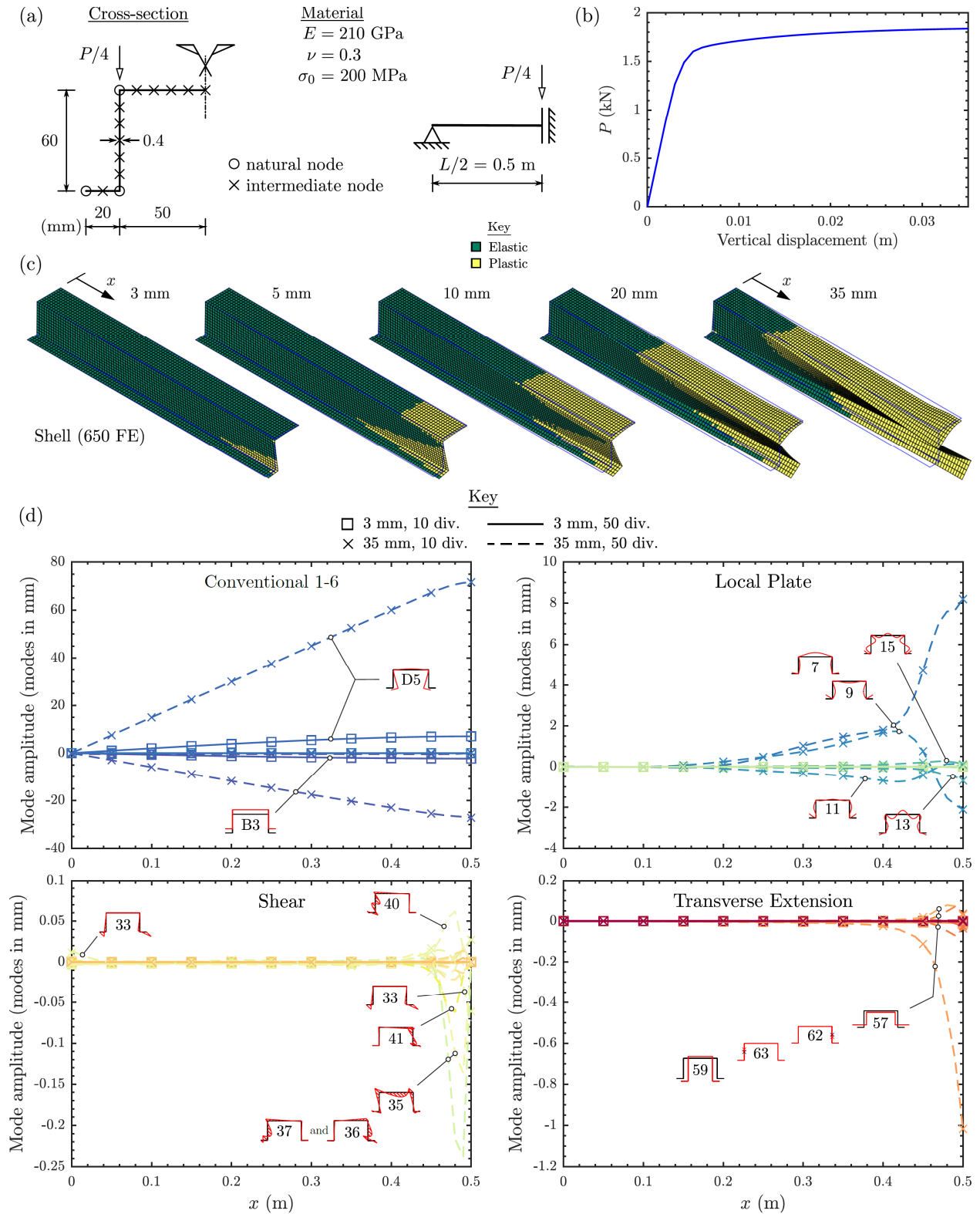


Figure 10: First-order analysis of an elastoplastic hat section beam: (a) geometry, loading, cross-section discretization and material parameters, (b) load-displacement path, (c) shell model deformed configurations and (d) GBT mode amplitude functions

(extension, bending, torsion, distortion, local-plate, etc.) while avoiding all issues. Note that strains are chosen instead of (elastic) stresses, since the latter are not suited to characterize elastoplastic stresses and yield a higher dimension basis (more stress components are generated due to Poisson effects) without any advantage.

The GBT membrane strains \mathbf{e} and curvatures $\boldsymbol{\chi}$ are obtained from Eq. (4), reading

$$\mathbf{e} = \begin{bmatrix} e_{xx} \\ e_{yy} \\ e_{xy} \end{bmatrix} = \begin{bmatrix} \bar{\mathbf{u}}^T \boldsymbol{\phi}_{,xx} \\ \bar{\mathbf{v}}_{,y}^T \boldsymbol{\phi} \\ (\bar{\mathbf{u}}_{,y} + \bar{\mathbf{v}})^T \boldsymbol{\phi}_{,x} \end{bmatrix}, \quad \boldsymbol{\chi} = \begin{bmatrix} \chi_{xx} \\ \chi_{yy} \\ 2\chi_{xy} \end{bmatrix} = - \begin{bmatrix} \bar{\mathbf{w}}^T \boldsymbol{\phi}_{,xx} \\ \bar{\mathbf{w}}_{,yy}^T \boldsymbol{\phi} \\ 2\bar{\mathbf{w}}_{,y}^T \boldsymbol{\phi}_{,x} \end{bmatrix}. \quad (8)$$

These relations can be written in terms of *strain modes* $\bar{e}_{ij}(y)$ and $\bar{\chi}_{ij}(y)$ as

$$\begin{cases} e_{ij} = \bar{\mathbf{e}}_{ij}^T(y) \boldsymbol{\phi}_{e_{ij}}(x) \\ \chi_{ij} = \bar{\boldsymbol{\chi}}_{ij}^T(y) \boldsymbol{\phi}_{\chi_{ij}}(x) \end{cases} \quad (i, j = x, y), \quad (9)$$

$$\begin{cases} \bar{\mathbf{e}}_{xx} = \bar{\mathbf{u}} \\ \bar{\mathbf{e}}_{yy} = \bar{\mathbf{v}}_{,y} \\ \bar{\mathbf{e}}_{xy} = \bar{\mathbf{u}}_{,y} + \bar{\mathbf{v}} \end{cases} \quad \begin{cases} \bar{\boldsymbol{\chi}}_{xx} = -\bar{\mathbf{w}} \\ \bar{\boldsymbol{\chi}}_{yy} = -\bar{\mathbf{w}}_{,yy} \\ 2\bar{\boldsymbol{\chi}}_{xy} = -2\bar{\mathbf{w}}_{,y} \end{cases} \quad (10)$$

where the column vectors $\bar{\mathbf{e}}_{ij}$ and $\bar{\boldsymbol{\chi}}_{ij}$ collect the strain modes, while the column vectors $\boldsymbol{\phi}_{e_{ij}}$ and $\boldsymbol{\phi}_{\chi_{ij}}$ gather the associated amplitude functions (the problem unknowns). In the geometrically linear case, the strains are linear functions of the displacement field derivatives and there is a relation between the various strain amplitude functions — for instance, from Eqs. (8) and (9), $\boldsymbol{\phi}_{e_{xx}} = \boldsymbol{\phi}_{,xx}$ and $\boldsymbol{\phi}_{e_{yy}} = \boldsymbol{\phi}$ —, but this does not hold in the geometrically non-linear case (the Green-Lagrange strains are quadratic functions of the displacement field derivatives). Since the warping functions of the shear type II modes coincide with those of the conventional bending, torsion (in open sections) and distortional modes (recall Section 3), duplicate $\bar{\mathbf{e}}_{xx}$ strain modes are obtained and must be discarded. For illustrative purposes, Fig. 11 shows the deformation and strain modes of a lipped channel. The discretization adopted leads to 15 conventional modes that generate 43 strain modes (their maximum absolute values are indicated in the figure).

The recovery of the strain mode amplitude functions from shell finite element analysis results relies on integration point strains and thus a regular shell mesh should be adopted, so that all integration points lie in the same cross-sections. For each cross-section, the following steps are carried out:

- (i) From the shell model results, the Green-Lagrange strains are obtained at all cross-section integration point, along the GBT local axes, $\mathbf{E}^T = [E_{xx} \ E_{yy} \ 2E_{xy}]$.
- (ii) For each integration point location along y , defined by $m = 1, \dots, M$, where M is the number of such locations, the membrane strains and curvatures are calculated from

$$\begin{cases} \mathbf{e} = (\mathbf{E}^{\text{top}} + \mathbf{E}^{\text{bottom}})/2 \\ \boldsymbol{\chi} = (\mathbf{E}^{\text{top}} - \mathbf{E}^{\text{bottom}})/(z^{\text{top}} - z^{\text{bottom}}) \end{cases} \quad (11)$$

where “top” and “bottom” designate the top and bottom integration points along z , respectively. Although the Green-Lagrange strains are non-linear along z , this approximation is acceptable for thin-walled members and small strains.

- (iii) The components \mathbf{e} and $\boldsymbol{\chi}$ are assembled in vectors \mathbf{e}_{ij} and $\boldsymbol{\chi}_{ij}$ (of dimension M). These vectors can be related to the GBT strain modes through the linear systems

$$\mathbf{e}_{ij} = \mathbf{T}_{e_{ij}} \boldsymbol{\phi}_{e_{ij}}, \quad \boldsymbol{\chi}_{ij} = \mathbf{T}_{\chi_{ij}} \boldsymbol{\phi}_{\chi_{ij}}, \quad (12)$$

where element mn of matrices $\mathbf{T}_{e_{ij}}$ or $\mathbf{T}_{\chi_{ij}}$ contains the value of strain mode \bar{e}_{ij} or $\bar{\chi}_{ij}$ number n at location m , whereas $\boldsymbol{\phi}_{e_{ij}}, \boldsymbol{\phi}_{\chi_{ij}}$ are the sought strain mode amplitudes.

- (iv) It is assumed that the shell cross-section discretization is more refined than the GBT one, hence the systems (12) are over-determined and are solved using the method of least squares.

4.4 Illustration of the strain mode recovery procedure

The first example concerns the simply supported lipped channel beam shown in Fig. 12(a), acted by a sinusoidally distributed transverse load. For a linear elastic material and small displacements, a GBT analytical solution is available (Garcea et al. 2016) and is employed to validate the proposed strain decomposition procedure. Only the conventional deformation modes are considered (see Fig. 11(b)), since the remaining ones have very small participations, and thus only the corresponding strain modes, displayed in Fig. 11(c), are used to retrieve the GBT solution from the shell model results. The shell model is shown in Fig. 12(b), having a regular mesh of 780 elements and a mid-span symmetry simplification. At the simple support, all cross-section in-plane displacements are restrained, whereas at mid-span the longitudinal displacements and the cross-section in-plane rotations are prevented. The results are presented in Figs. 12(b)-(c). Fig. 12(b) displays the deformed configurations obtained with the GBT analytical solution and the shell model (U_Y is the mid-span web maximum displacement), evidencing an excellent agreement. The graphs in Fig. 12(c) plot the analytical and recovered strain mode amplitude functions and prompt the following remarks:

- (i) All strain mode amplitude functions are in excellent agreement (most of them virtually coincide), thus validating the proposed procedure. Some differences are observed near the support, mostly for $\boldsymbol{\phi}_{\chi_{xx}}$, due to restrained Poisson effects in the shell model, since these effects are discarded in the GBT analytical solution with conventional modes.
- (ii) Although 15 deformation modes have been considered, only three of them have significant participations in the solution, namely modes B3, D5 and LP7.

The proposed recovery procedure is applied next to a well-known benchmark problem for testing shell finite elements (Chrosielewski et al. 1992, Eberlein & Wriggers 1999). The problem parameters are provided in Fig. 13(a) (σ_0 is the yield stress), while Fig. 13(b) compares the elastic and elastoplastic load-displacement paths reported by Eberlein & Wriggers (1999) with those obtained with the present implementation of the MITC-4 element, using the same discretization — clearly, an excellent match is observed. The GBT cross-section discretization (see Fig. 13(a)) leads to the strain modes displayed in Fig. 13(c), which are scaled to obtain unit absolute maximum strains, so that each strain mode amplitude function has a clear physical meaning: it provides the absolute maximum strain at each cross-section, caused by the associated strain mode.

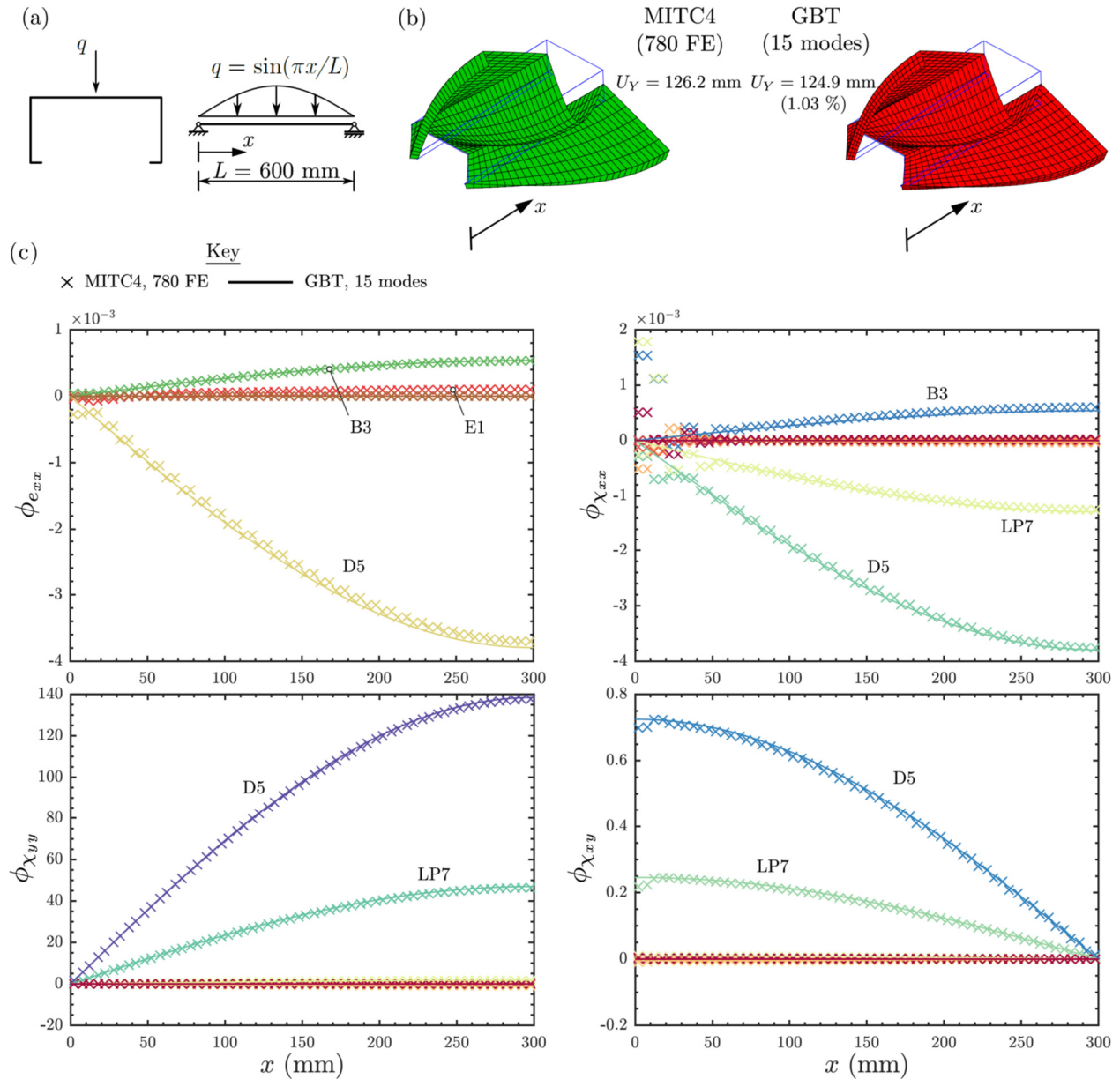


Figure 12: Lipped channel beam: (a) loading, (b) deformed configurations and (c) GBT strain mode amplitudes

A linear elastic analysis is first carried out. A 0.25 mm vertical displacement of the load application point is enforced, corresponding to $P = 21.8 \text{ kN}$. The results of the recovery procedure are presented in Fig. 14 and are compared with the analytical solution provided by the Vlasov beam theory for a cantilever subjected to major-axis bending and torsion, which is indicated by the “X” symbols in the graphs. These graphs prompt the following remarks:

- (i) The recovered strains $\phi_{e,xx}$ and $\phi_{\chi,xy}$ match extremely well the analytical solutions. For the former, the remaining modes have negligible amplitudes, whereas for the latter, besides torsion, LP6 has also a noteworthy participation for $x/L > 0.8$, revealing significant local-plate bending, in accordance with the $\phi_{\chi,yy}$ graph (LP8 and LP10 also have relevant participations).

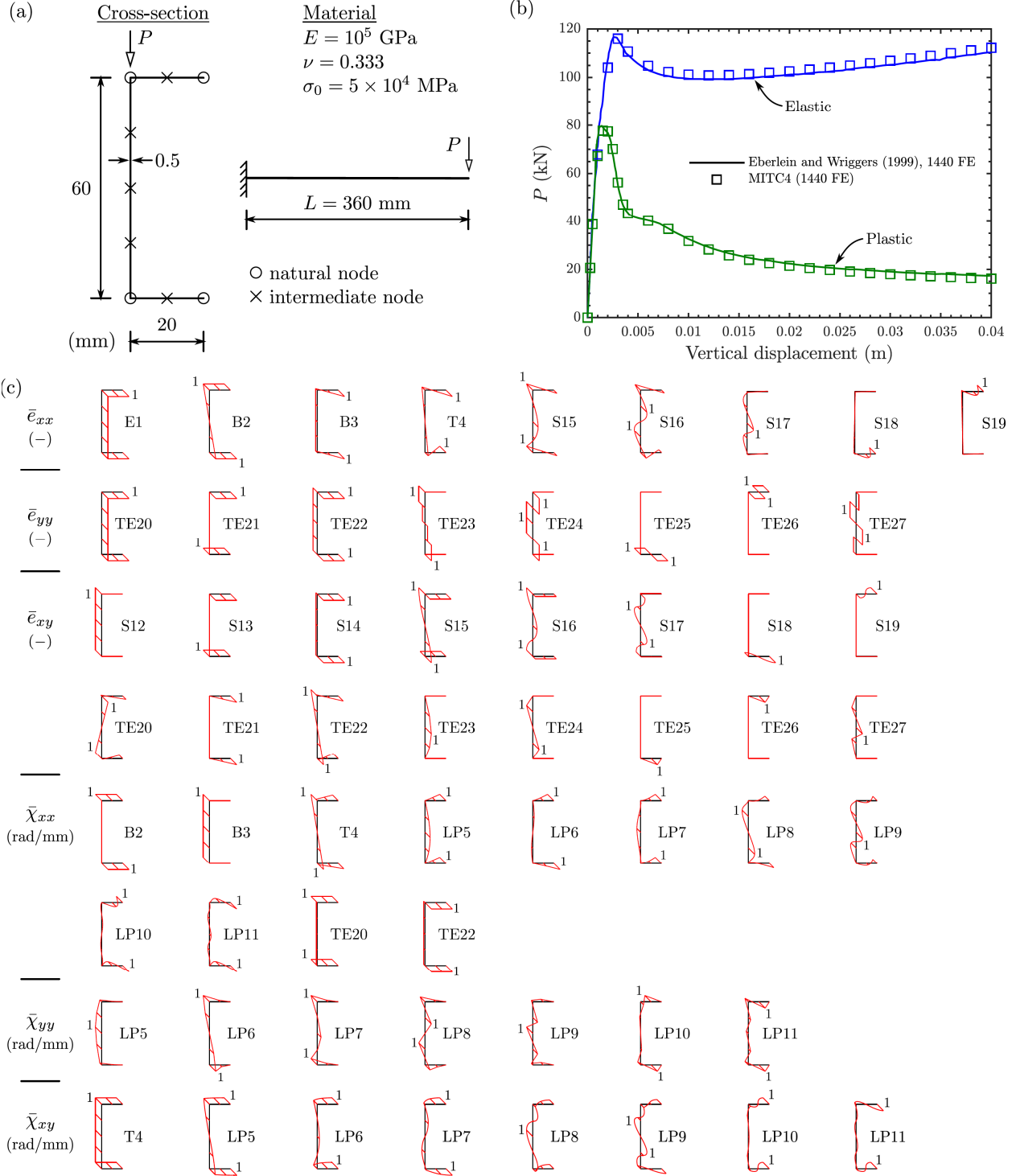


Figure 13: Plain channel cantilever: (a) geometry, cross-section discretization and loading, (b) load-displacement diagram and (c) GBT strain modes

(ii) In general, significant end effects are observed for all strain components, except for $\phi_{e_{xx}}$. In some graphs these effects are restricted to very short lengths, namely for $\phi_{e_{yy}}$ and $\phi_{e_{xy}}$.

GBT modal strain amplitudes

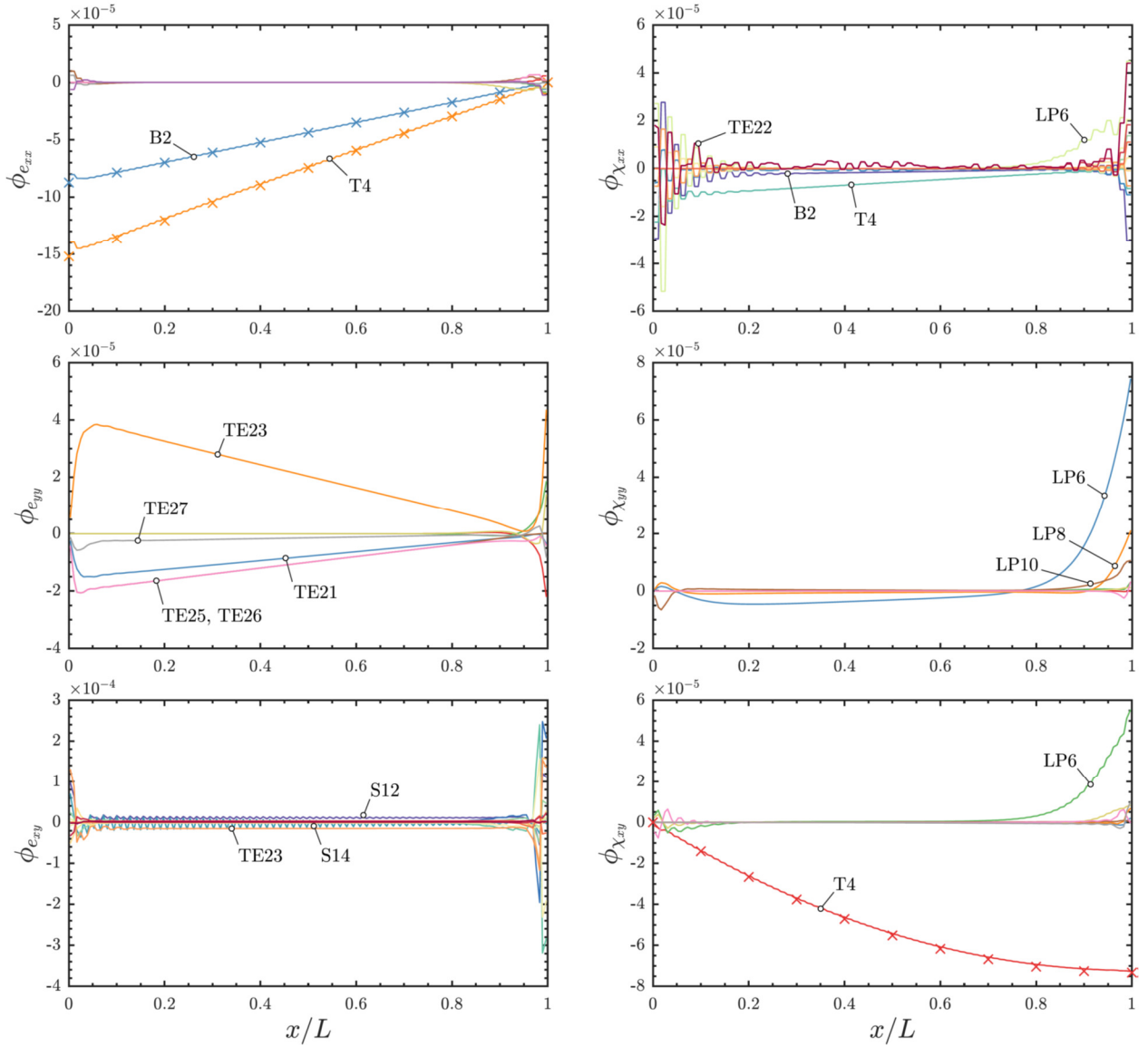


Figure 14: Plain channel cantilever GBT strain mode amplitudes for the linear elastic case ($P = 21.8 \text{ kN}$)

- (iii) The $\phi_{e_{yy}}$ graph shows that Poisson effects due to bending and torsion are mainly captured by four transverse extension modes (21, 23, 25 and 26) — note that their amplitude functions follow those of $\phi_{e_{xx}}$. The fact that four TE modes are required to replicate the Poisson effects due to B2 and T4 is not surprising, since GBTUL does not calculate TE modes on the basis of this effect (nevertheless, note that only four modes are required).
- (iv) Returning to the $\phi_{e_{xy}}$ graph and neglecting end effects, the most relevant modes are S12 and S14, which correspond to the shear strains due to major-axis bending and torsion, respectively, and TE23, which further refines the web strains associated with bending. Therefore, as expected, the strains are due to vertical shear and bi-shear. A slight oscillation is observed for modes S12 and S14 (this issue is addressed in the next example).
- (v) Concerning $\phi_{\chi_{xx}}$ and neglecting again end effects, the most relevant modes are once more major-axis bending (B2) and torsion (T4), together with LP6, as discussed in item (i) above.

The elastic large displacement analysis case is now dealt with. Fig. 15 displays (i) four successive deformed configurations and (ii) the recovered GBT strain mode amplitudes associated with a 0.040 m vertical displacement of the load application point. The deformed configurations reveal that this is a quite peculiar problem, in which lateral-torsional buckling triggers local buckling of the top flange. The strain mode amplitude graphs are significantly more complex than those of the linear solution and the following remarks are appropriate:

- (i) For $\phi_{e_{xx}}$, all associated strain modes are relevant except axial extension (obviously), with the higher-order strains (S15-19) being the most relevant. Naturally, torsion (T4) is maximum at the support and null at the free end, with the opposite occurring for $\phi_{\chi_{xy}}$. The bending mode (B2 and B3) amplitude function shapes reflect the twisting effect towards the free end — as the section rotates, B2 decreases and B3 increases (both are obviously null at the free end).
- (ii) The $\phi_{\chi_{xx}}$, $\phi_{\chi_{yy}}$ and $\phi_{\chi_{xy}}$ graphs show that local-plate deformation occurs throughout the beam. The corresponding deformed configuration (0.040 m) exhibits three short-wavelength outward buckles at the top flange, located at $x/L \approx 0.13, 0.28, 0.61$ and preceded by inward buckles. This is in perfect agreement with the $\phi_{\chi_{xx}}$ graph, which displays short wavelength upward/downward peaks corresponding to the inward/outward buckles, respectively, the latter occurring at the identified locations. These buckles can also be identified in the $\phi_{\chi_{yy}}$ graph (*e.g.*, see the LP10 function), but a more complex behavior is portrayed. In particular, LP5 has a dominant participation for $x/L > 0.5$, revealing significant web outward transverse bending. The local buckles can also be observed in the $\phi_{\chi_{xy}}$ graph, but the peaks/zeros correspond to the zeros/peaks of $\phi_{\chi_{xx}}$, respectively, since χ_{xx} essentially depends on $\phi_{,xx}$, whereas χ_{xy} depends on $\phi_{,x}$ for the small displacement elastic case (recall Eq. (8)).
- (iii) The $\phi_{e_{yy}}$ and $\phi_{e_{xy}}$ graphs are much more complex than their linear counterparts (see Fig. 14), reflecting the higher complexity of the deformed configuration. Nevertheless, the $\phi_{e_{yy}}$ graph shows peaks corresponding to the inward/outward buckles discussed in item (ii) and highly localized strains at the free end. Concerning $\phi_{e_{xy}}$, the local buckling peaks are roughly observed, as the amplitude functions are quite complex, with alternating peaks in adjacent integration points. This is not a deficiency of the proposed recovery procedure, but instead a feature of the shell model solution, which also exhibits this behavior. If the strains are averaged in each shell element, the graph (not shown) becomes smooth, but the most relevant strain components are those already detected in the graph shown (S13, S15, S19, TE20 and TE21).

The results for the elastoplastic large displacement analysis are reported in Fig. 16. As before, the GBT strain mode amplitudes are recovered for a 0.040 m vertical displacement of the load application point. The deformed configurations reveal the emergence of a pronounced local buckle near the support and several small buckles throughout the beam. The yellow zones indicate shell elements with at least one yielded integration point. Although the strain mode amplitude graphs are much more complex than the previous ones, due to the large displacements and plastic strains involved, it is still possible to draw the following conclusions:

- (i) For $\phi_{e_{xx}}$ all modes participate in the solution, including axial extension, due to its coupling with bending in the elastoplastic range.

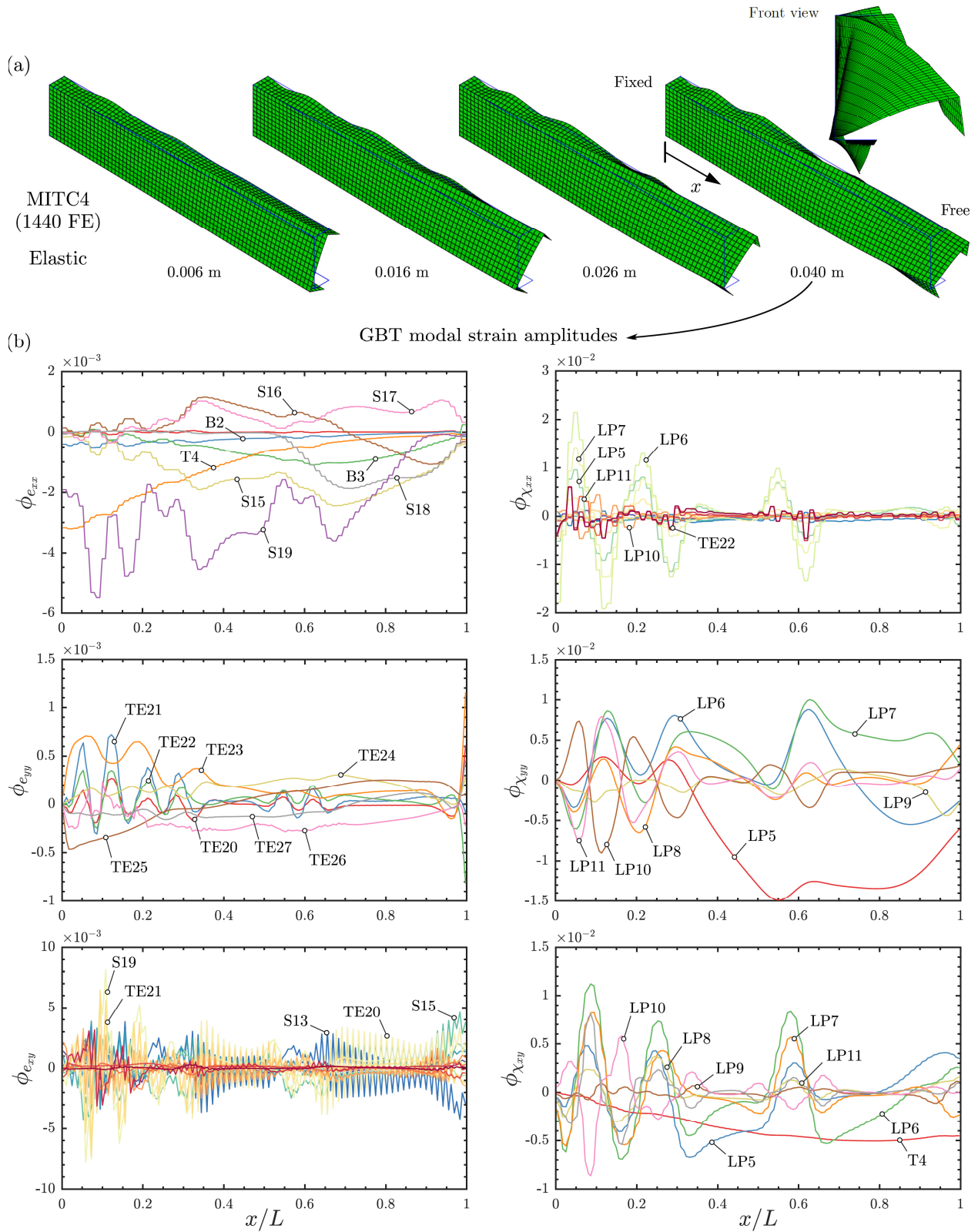


Figure 15: Plain channel elastic cantilever (a) deformed configurations and (b) GBT strain mode amplitudes

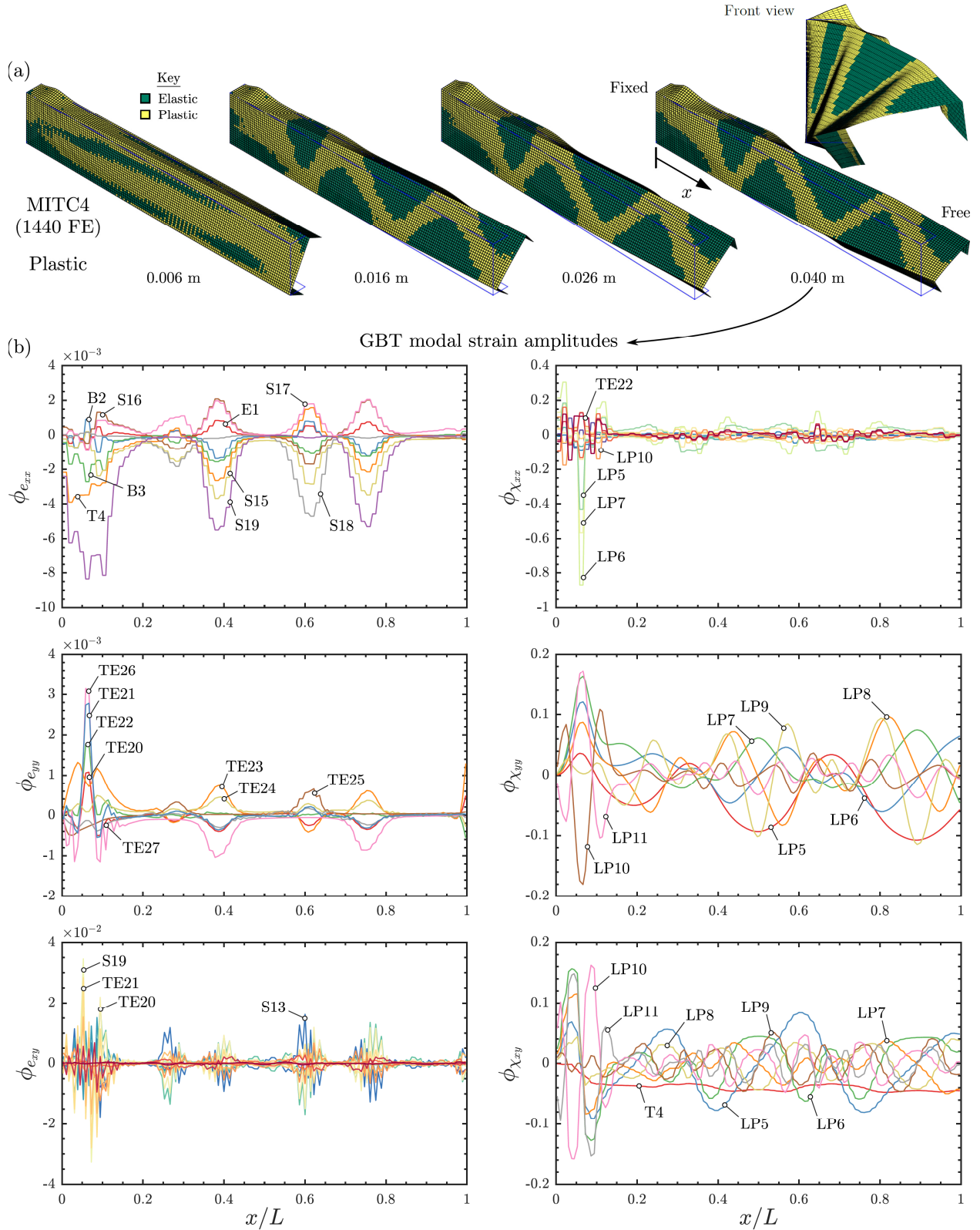


Figure 16: Plain channel elastoplastic cantilever (a) deformed configurations and (b) GBT modal strain amplitudes

- (ii) All three membrane strain graphs exhibit five peaks at the same x/L locations, corresponding to the yellow zones near the top/bottom flanges in the 0.040 m deformed configuration.
- (iii) The three curvature graphs evidence highly complex local-plate strains. Nevertheless, it is worth noting that the pronounced local buckling at the top flange, near the built-in end, is clearly observed in all of them.

The last illustrative example concerns the hat-section cantilever shown in Fig. 17(a). The GBT cross-section discretization leads to the strain modes in Fig. 17(c), which are scaled to obtain unit absolute maximum strains. This cross-section was selected because it has more fold lines than the preceding one and, therefore, is susceptible to distortion (modes D5 and D6). The elastic and elastoplastic load-displacement paths obtained with 1950 shell elements are plotted in Fig. 17(b).

The elastic results are reported in Fig. 18, which includes (i) four successive deformed configurations and (ii) the recovered GBT strain mode amplitudes, obtained using the proposed procedure, for a 0.145 m vertical displacement of the load application point. Concerning the deformed configurations, it is observed that the beam undergoing bending and torsion at the early loading stages, before local and distortional deformation gradually emerge and develop. For 0.145 m, the cross-section deformation is highly complex, involving (i) distortion throughout the whole beam, with a pronounced buckle near $x/L = 0.25$, (ii) one/two local buckles of the left/right lips, respectively, near the support, and (iii) a (top) flange local buckle at $x/L \approx 0.65$. The strain mode amplitude graphs essentially quantify these behavioral features:

- (i) Torsion-bending (T4-B3) is clearly visible in the $\phi_{e_{xx}}$ and $\phi_{e_{xy}}$ graphs. The former shows that the relevance of these modes increases near the localized distortional “bulge” ($x/L = 0.25$).
- (ii) The distortional deformations are detected in $\phi_{e_{xx}}$, $\phi_{\chi_{yy}}$ and $\phi_{\chi_{xy}}$. It is observed that the localized distortion in the vicinity of $x/L = 0.25$ is asymmetric, due to the presence of both D5 and D6, and that symmetric distortion (D5) extends throughout the whole beam.
- (iii) The complex local-plate deformation pattern can be observed in $\phi_{\chi_{yy}}$ and $\phi_{\chi_{xy}}$ (the latter has opposing peaks/zeros with respect to the former), with clearly visible local buckles in the lips, near the support, and flange, at $x/L \approx 0.65$. It is further observed that the local-plate modes also participate in the region with localized distortional deformations ($x/L = 0.25$). Similar conclusions can be drawn from $\phi_{\chi_{xx}}$, but its high complexity prevents acquiring further structural insight.
- (iv) As in the previous example, the $\phi_{e_{yy}}$ and $\phi_{e_{xy}}$ graphs are quite complex, due to the large displacements involved. Nevertheless, out of the total number of strain modes (13 for \bar{e}_{yy} and 26 for \bar{e}_{xy}), these strain fields essentially involve 7-8 modes: (i) TE31, TE32, TE35-38 and TE40, for \bar{e}_{yy} , and (ii) S18-21, S23, TE30, TE34 and TE36, for \bar{e}_{xy} .

Finally, the elastoplastic behavior of the hat-section cantilever shown in Fig. 17(a) is addressed (see Fig. 19). The GBT strain mode amplitudes displayed concern a 0.150 m vertical displacement of the load application point. The deformed configurations make it possible to conclude that yielding first develops at the support and gradually spreads throughout the beam, with increasing bending-torsion deformations and a pronounced local buckle appearing in the left lip and web, next to the support. The front view shows several small local buckles in the flange, at $x/L > 0.5$, and symmetric distortion at the free end section. The strain amplitude graphs in this case are quite

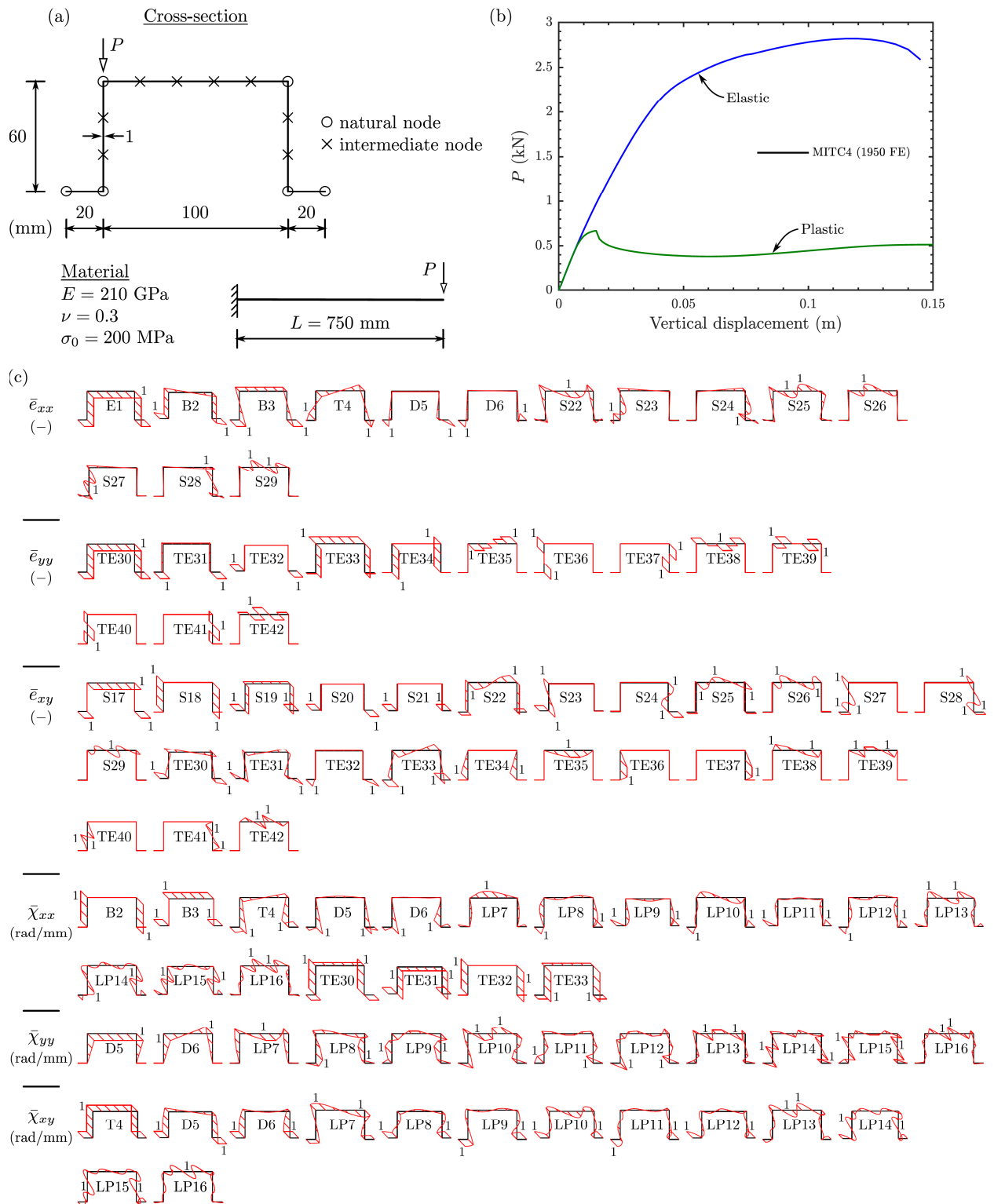
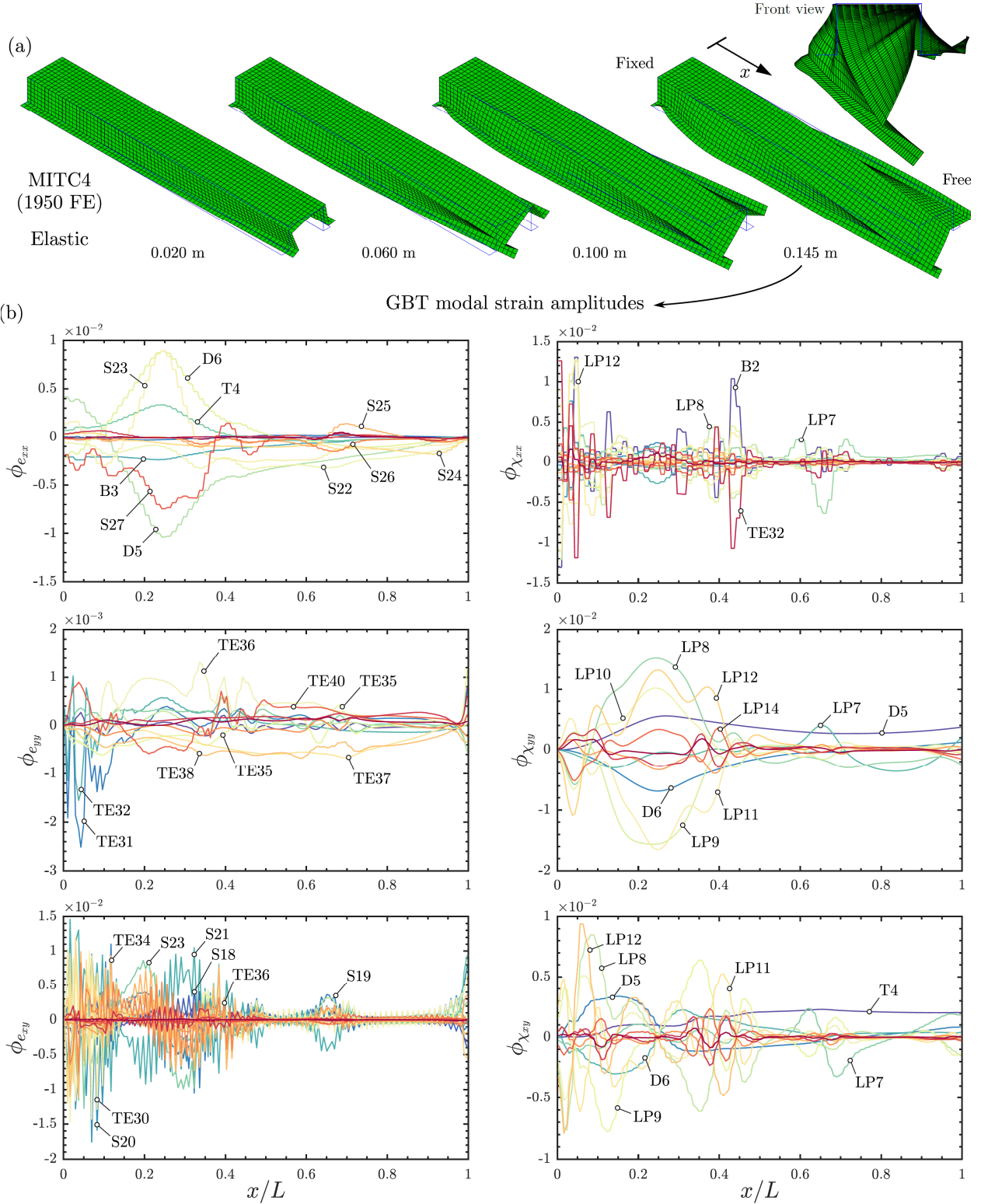


Figure 17: Hat-section cantilever: (a) geometry, cross-section discretization and loading, (b) load-displacement diagram and (c) GBT strain modes



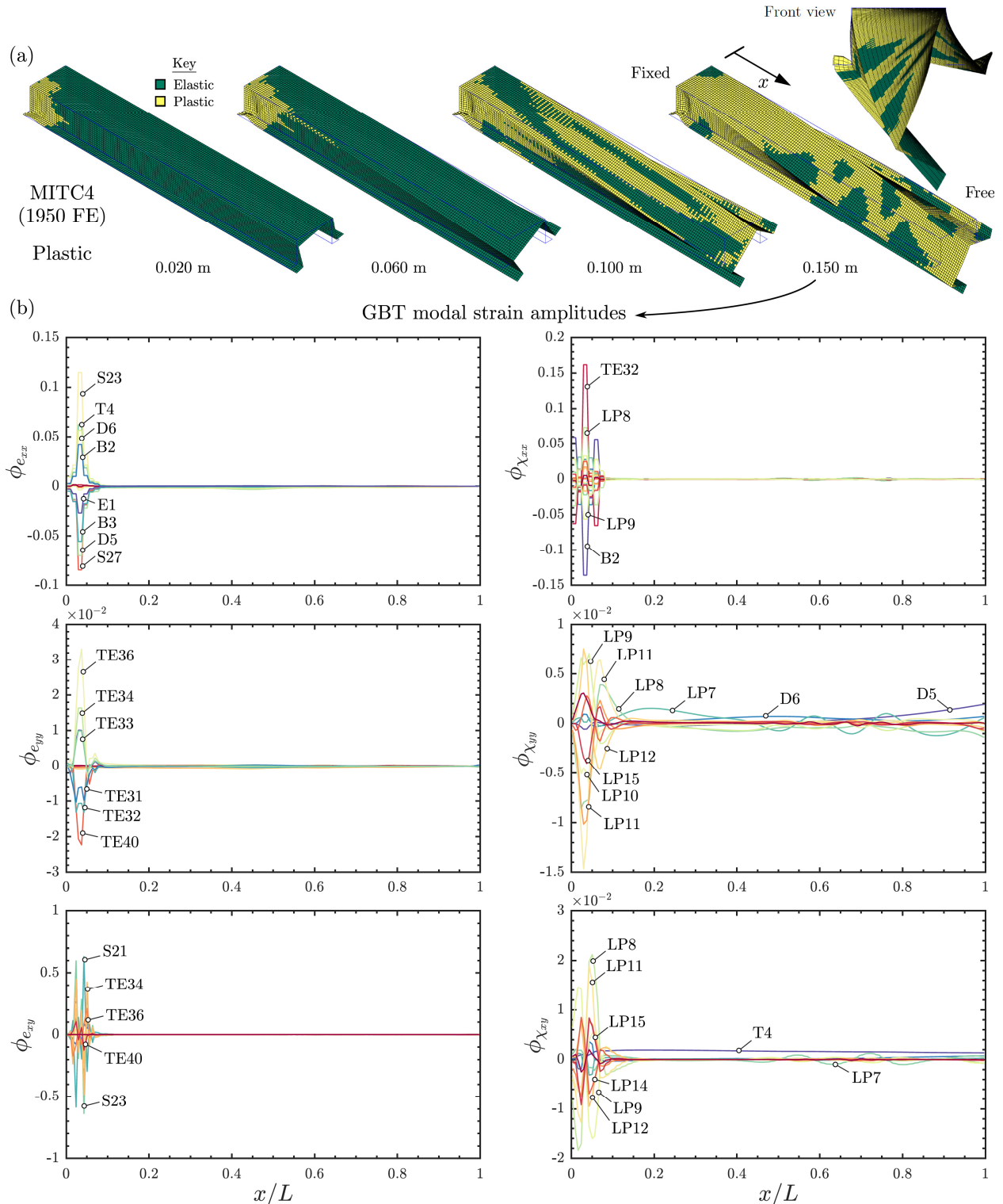


Figure 19: Elastoplastic hat-section cantilever (a) deformed configurations and (b) GBT strain mode amplitudes

simple and reflect precisely the features just described: (i) all graphs provide evidence of local buckles near the support, (ii) $\phi_{\chi_{yy}}$ shows that D5, D6 and LP7 extend throughout the whole beam, with LP7 exhibiting several waves for $x/L > 0.5$ and (iii) $\phi_{\chi_{xy}}$ corroborates the previous assertion

concerning LP7 and also reveals that torsion (T4) is uniform rather than non-uniform, due to yielding.

5. Combining shell and geometrically exact beam elements

This section is devoted to presenting a modeling approach for thin-walled structures that combines shell and geometrically exact beam finite elements including cross-section deformation, making it possible to carry out computationally efficient large displacement elastic and elastoplastic analyses. Since the adopted beam element is capable of handling moderate cross-section deformation, a two-step procedure is herein proposed: (i) in the first step an (elastic or elastoplastic) analysis is carried out using only beam finite elements including just a few deformation modes, to estimate the extent of the zones undergoing cross-section deformation and/or plastic strains, and then (ii) an analysis is carried out, using shell elements in the previously identified zones, and beam elements elsewhere, to ensure computational efficiency gains with respect full shell models. Ideally, the procedure should be applied in an adaptive fashion — *i.e.*, the model should be updated within the incremental/iterative analysis, replacing at each load/displacement increment beam elements by shell elements as cross-section deformation and/or plasticity spreads —, but this requires ensuring compatibility between elements in the through-thickness direction, which involves a significant computational cost when using the adopted beam element. This is because the beam kinematic description, given by Eq. (2), does not rely on through-thickness director vectors \mathbf{v}_n , like the shell model (recall Eq. (1)), and therefore a constraint equation involving these directors is rather complex. For this reason, only the mid-surface nodes are constrained in this work, which means that, in the combined shell-beam model, the beam element must not include cross-section deformation modes involving transverse plate bending. However, recall that a preliminary analysis is carried out to detect the zones where such deformation occurs.

The constraint equations are of the form

$$U_j^s - U_j^b = 0, \quad (13)$$

where U_j^s and U_j^b are the constrained mid-surface displacements of the shell and beam elements, respectively, along direction j . These constraints are enforced through the Lagrange multiplier approach, which amounts to adding work terms $\zeta(U_j^s - U_j^b)$. The virtual variation and ensuing incremental/iterative linearization are added to the equilibrium equations and tangent stiffness matrix, respectively, and read

$$\delta\zeta(U_j^s - U_j^b) + \zeta(\delta U_j^s - \delta U_j^b), \quad (14)$$

$$\delta\zeta(\Delta U_j^s - \Delta U_j^b) + \Delta\zeta(\delta U_j^s - \delta U_j^b) + \zeta\Delta\delta U_j^b, \quad (15)$$

where advantage was taken from the fact that $\Delta\delta U_j^s = 0$, since only the mid-surface displacements are constrained. To proceed, the following relations are introduced

$$\delta U_j^b = \mathbf{\Xi}_{DU_b} \delta \mathbf{d}_b, \quad (16)$$

$$\Delta U_j^b = \mathbf{\Xi}_{DU_b} \Delta \mathbf{d}_b, \quad (17)$$

$$\delta U_j^s = \mathbf{1}^T \delta \mathbf{d}_s, \quad (18)$$

$$\Delta U_j^s = \mathbf{1}^T \Delta \mathbf{d}_s, \quad (19)$$

$$\Delta \delta \mathbf{U}_b \cdot \mathbf{E}_j = (\delta \mathbf{d}_b)^T \mathbf{\Xi}_{D^2 U_b} \Delta \mathbf{d}_b \quad (20)$$

where \mathbf{d}_b and \mathbf{d}_s are column vectors that collect the beam and shell DOFs, respectively, $\mathbf{1}$ is a column vector whose only non-null entry equals 1 and has a position matching that of U_j^s in \mathbf{d}^s , the auxiliary matrices $\mathbf{\Xi}_{DU_b}$, $\mathbf{\Xi}_{D^2 U_b}$ are determined further ahead and $\mathbf{U}_b \cdot \mathbf{E}_j = U_j^b$ (\mathbf{E}_j is the relevant basis vector). With these relations, the equilibrium equations are solved using the Newton-Raphson method with (for simplicity the system below corresponds to a single constraint equation)

$$\begin{bmatrix} \mathbf{K}_s & \mathbf{0} & -\mathbf{1} \\ \mathbf{0} & \mathbf{K}_b - \zeta \mathbf{\Xi}_{D^2 U_b} & \mathbf{\Xi}_{DU_b}^T \\ -\mathbf{1}^T & \mathbf{\Xi}_{DU_b} & 0 \end{bmatrix} \begin{bmatrix} \Delta \mathbf{d}_s \\ \Delta \mathbf{d}_b \\ \Delta \zeta \end{bmatrix} = \begin{bmatrix} \mathbf{g}_s + \zeta \mathbf{1} \\ \mathbf{g}_b - \zeta \mathbf{\Xi}_{DU_b}^T \\ U_k^s - U_j^b \end{bmatrix}, \quad (21)$$

where \mathbf{K}_b and \mathbf{K}_s are the stiffness matrices of the shell and beam substructures, respectively, \mathbf{g}_b and \mathbf{g}_s are the corresponding out-of-balance force vectors, $U_j^s = \mathbf{1}^T \mathbf{d}_s$ and U_j^b is obtained from Eq. (2), *viz.*

$$\mathbf{U}_b = \mathbf{x} - \mathbf{x}_0 = \hat{\mathbf{u}} + \hat{\Lambda} \Lambda_0 (\mathbf{l}_0 + \mathbf{R} \sum_{i=1}^D \hat{p}^{(i)} \boldsymbol{\chi}^{(i)}) - \Lambda_0 \mathbf{l}_0. \quad (22)$$

where $\hat{\mathbf{u}} = \mathbf{r} - \mathbf{r}_0$ is the displacement of the cross-section center C . For a single element, collecting the independent kinematic parameters in vector

$$(\mathbf{d}_b)_e^T = [\hat{\mathbf{u}}^T \quad \hat{\boldsymbol{\theta}}^T \quad \hat{p}^{(1)} \quad \dots \quad \hat{p}^{(D)}], \quad (23)$$

the auxiliary matrices read

$$\mathbf{\Xi}_{DU_b} = \mathbf{E}_j^T [\mathbf{I} \quad \mathbf{\Xi}_{D\hat{\Lambda}}(\Lambda_0 \mathbf{l}) \quad \hat{\Lambda} \Lambda_0 \mathbf{R} \boldsymbol{\chi}^{(1)} \quad \dots \quad \hat{\Lambda} \Lambda_0 \mathbf{R} \boldsymbol{\chi}^{(D)}], \quad (24)$$

$$\mathbf{\Xi}_{D^2 U_b} = \begin{bmatrix} \mathbf{0}_{3 \times 3} & \mathbf{0}_{3 \times 3} & \mathbf{0}_{3 \times 1} & \dots & \mathbf{0}_{3 \times 1} \\ \mathbf{\Xi}_{D^2 \hat{\Lambda}}(\Lambda_0 \mathbf{l}, \mathbf{E}_j) & \mathbf{\Xi}_{D\hat{\Lambda}}^T(\Lambda_0 \mathbf{R} \boldsymbol{\chi}^{(1)}) \mathbf{E}_j & \dots & \mathbf{\Xi}_{D\hat{\Lambda}}^T(\Lambda_0 \mathbf{R} \boldsymbol{\chi}^{(D)}) \mathbf{E}_j \\ \mathbf{Sym.} & \mathbf{0} & \dots & \mathbf{0} \\ & & \ddots & \vdots \\ & & & \mathbf{0} \end{bmatrix}, \quad (25)$$

where matrices $\mathbf{\Xi}_{D\hat{\Lambda}}$ and $\mathbf{\Xi}_{D^2 \hat{\Lambda}}$ were originally introduced by Ritto-Corrêa & Camotim (2002), being worth noting that they are non-linear functions of the rotation vector $\hat{\boldsymbol{\theta}}$.

For illustrative purposes, the proposed method is applied to the analysis of the plain channel cantilever beam shown in Fig. 20(a), which undergoes severe cross-section deformation near the support, for large displacements. The cross-section discretization leads to 21 GBT deformation modes (1-9 conventional, 10-15 shear and 16-21 transverse extension) but, due to the problem symmetry, only the symmetric local-plate modes displayed in Fig. 20(b) (LP5, LP7 and LP9) are included in the beam element.

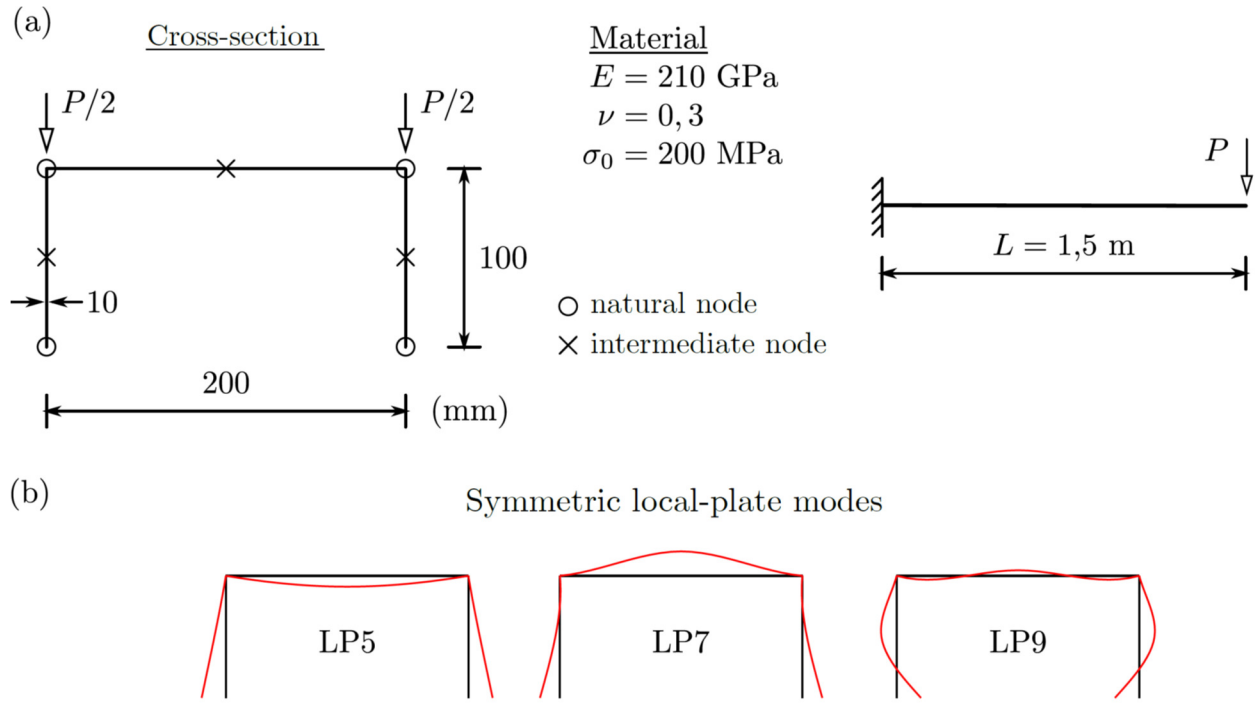


Figure 20: Symmetrically loaded plain channel cantilever: (a) geometry, material parameters, cross-section discretization and loading, and (b) GBT symmetric local-plate modes

The elastic analysis is first addressed. Fig. 21 shows the equilibrium paths and deformed configurations obtained with (i) a refined shell model involving 1500 MITC-4 elements, (ii) 5 equal-length geometrically exact beam elements (GEB), including either no deformation modes or the three local-plate modes in Fig. 20(b), and (iii) two combined GEB-shell models (300 MITC-4 + 4 GEB and 600 MITC + 4 GEB). The deformed configurations obtained with 5 GEB without deformation modes are not shown since they only exhibit bending. These results prompt the following remarks:

- (i) Consider first the results obtained with the GEB models. Without deformation modes, the linear part of the equilibrium path is accurately captured, but the model fails to detect the onset of local buckling for $P \approx 110 \text{ kN}$. With only three local-plate modes, the model detects quite accurately this point, but captures poorly the subsequent equilibrium path and slightly overpredicts the extent of buckling near the support. Nevertheless, this model is useful to estimate the beam length that needs to be modelled with shell elements, as discussed next.
- (ii) The combined GEB-shell model with 300 MITC-4 elements (corresponding to replacing the first GEB element with shell elements) performs better than the GEB model with three deformation modes but is unable to capture accurately the shell model non-linear equilibrium path and deformed configurations. In particular, a smaller buckled zone is predicted and therefore a stiffer path equilibrium is obtained (namely for displacements above 0.2 m).
- (iii) The combined GEB-shell model with 600 MITC-4 elements — corresponding to replacing the first two GEB elements with shell elements, the buckled zone predicted by the GEB model with deformation modes) — leads to an equilibrium path and deformed configurations that practically match the full shell model ones for the whole displacement range considered, thus highlighting the advantages of the proposed procedure.

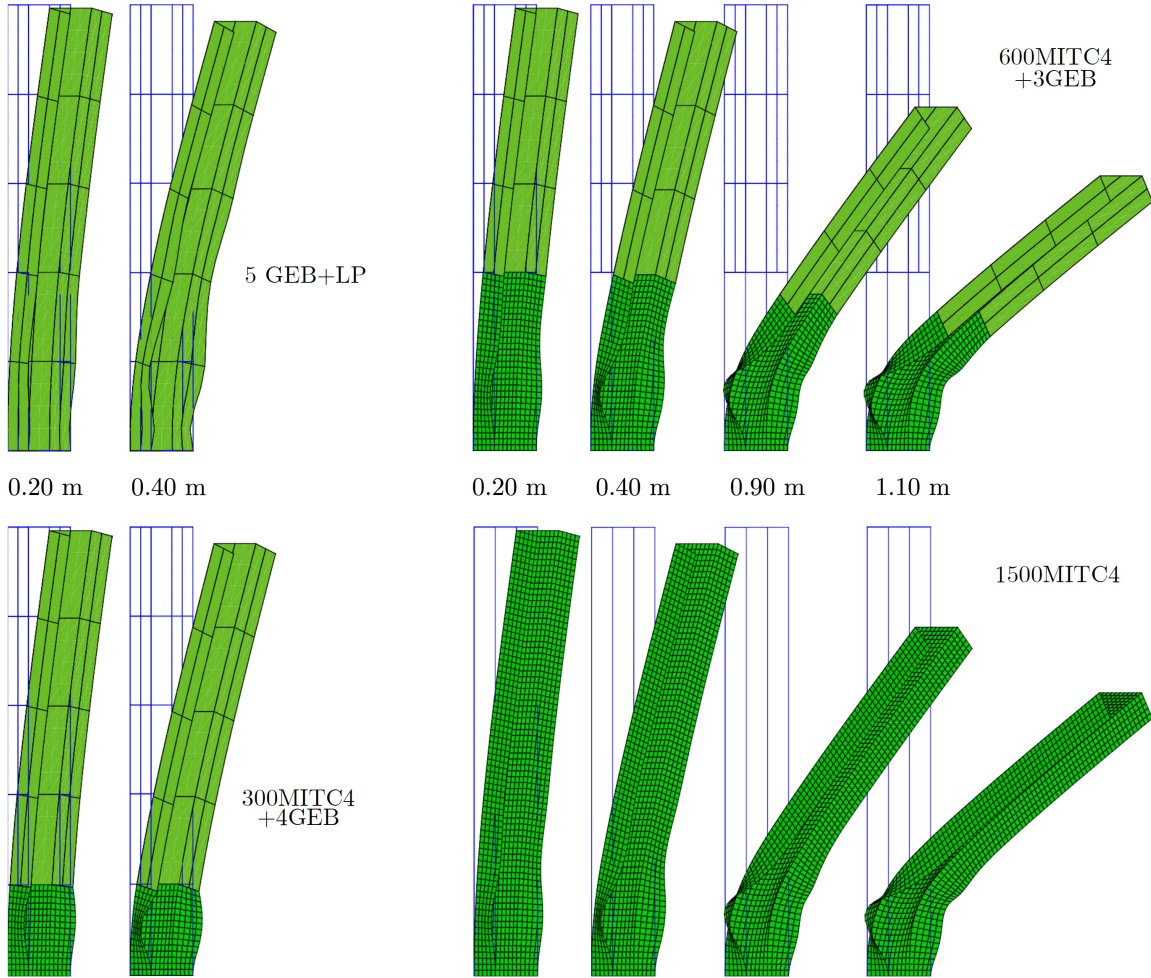
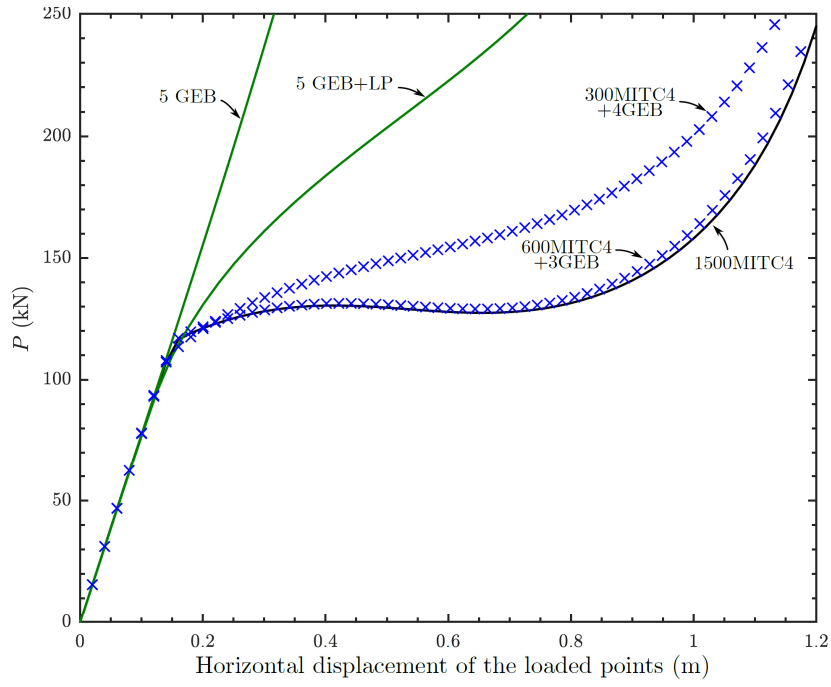


Figure 21: Elastic symmetrically loaded plain channel load-displacement graph and deformed configurations

Consider now the elastoplastic analysis, whose results obtained with a full shell model (1500 MITC-4) and a combined model with 300 MITC-4 + 4 GEB elements are shown in Fig. 22. Note that the combined model has fewer shell elements because plasticity leads to a higher localization of cross-section deformation. These results show that the proposed procedure, based on the combination of shell and GEB elements leads to excellent results throughout the whole (large) displacement range considered, reproducing accurately the severe localized elastoplastic deformations occurring near the support.

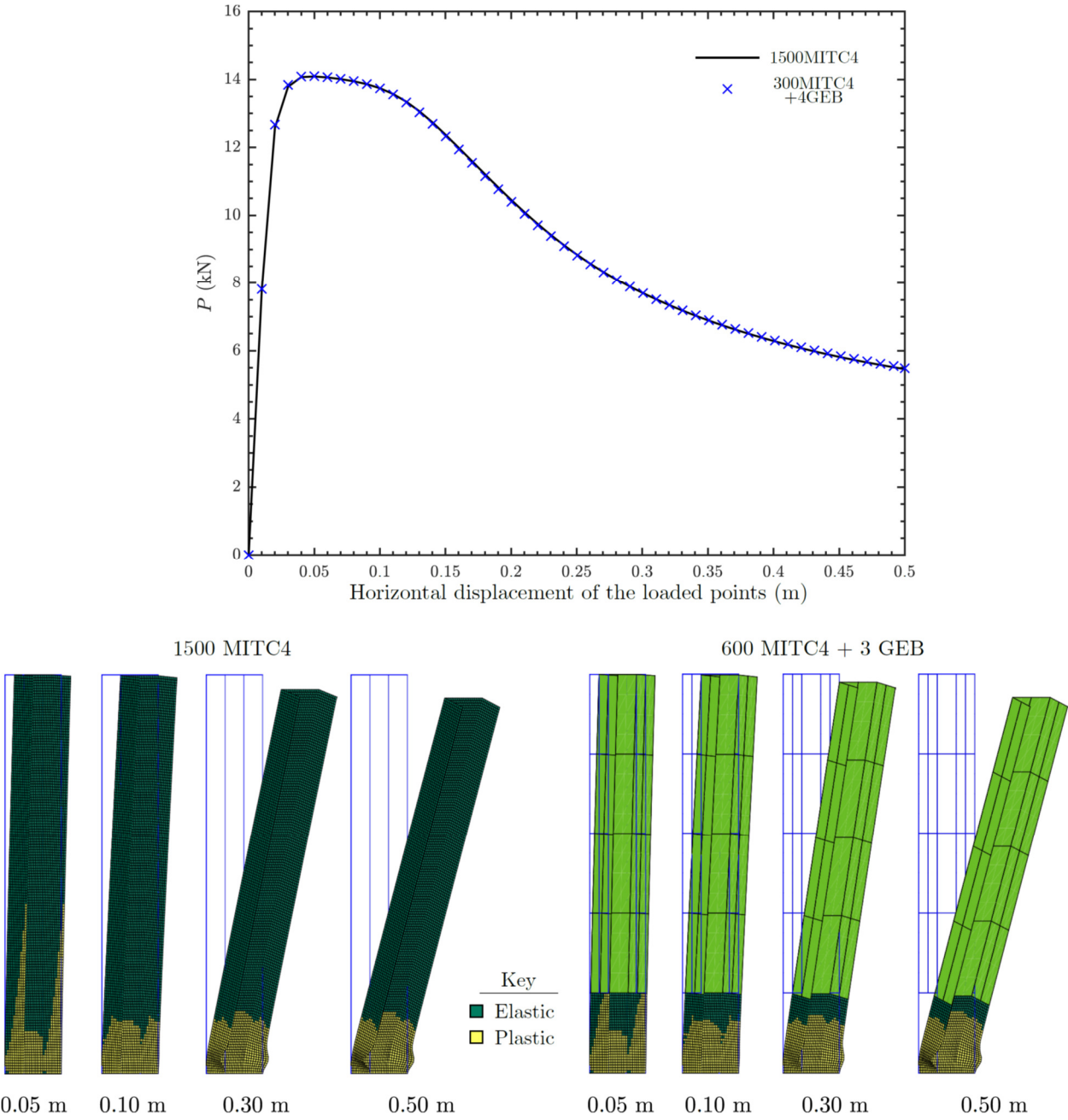


Figure 22: Elastoplastic symmetrically loaded plain channel load-displacement graph and deformed configurations

6. Conclusion

This paper extended previous work by the authors, intended to contribute towards a more efficient modeling of thin-walled members and frames, by presenting, validating and illustrating the application of two approaches that combine the advantages of Generalized Beam Theory (GBT) — in-depth understanding of the mechanical behavior of the structural system under analysis, obtained from the modal decomposition of the solution — and conventional shell finite elements — versatility and reduced computational effort in non-linear problems. In particular:

- (i) The first approach consists of a procedure that recovers the GBT deformation mode participations through post-processing shell finite element results. The procedure covers all GBT cross-section deformation mode families, can be used in several analysis types (bifurcation, vibration, first-order elastic and elastoplastic) of thin-walled structural systems with complex geometries (*e.g.*, having tapered/curved segments and joints) and is also applicable to finite strip buckling results. Its extension to elastic/elastoplastic large displacement analyses was also addressed, which required introducing the “GBT cross-section strain mode” concept, to circumvent the fact that the GBT deformation modes are not suitable to describe finite rotations. It should be emphasized that the proposed procedure is extremely useful in problems for which beam elements including cross-section deformation cannot be employed or their use is not computationally competitive. Moreover, since its implementation in existing finite element programs (namely commercial programs) is quite straightforward, the authors believe that it has a great potential for application in structural design, since it enables the reinterpretation of shell finite element (or finite strip) results in the light of GBT.
- (ii) The second approach consists of combining beam and shell elements in the same model. In this work this concept was extended to enable the performance of large displacement elastic and elastoplastic analyses. In this displacement range GBT-based finite elements cannot be employed and thus the geometrically exact beam element developed by Peres et al. (2021), which incorporates GBT cross-section deformation modes, was used instead. In the proposed procedure, the beam elements are employed to detect the zones undergoing localized or plastic deformation, which are subsequently re-meshed using shell elements (much more efficient in such zones), to obtain significant computational savings. Ideally, this procedure should be applied adaptively, updating the finite element model within the incremental/iterative analysis, replacing at each step the beam elements with shell elements as localized deformations and/or plasticity spread.

All the illustrative numerical examples presented throughout the paper clearly show that the proposed procedures enable a significant reduction of the computational effort, while enabling the acquisition of in-dept insight on the mechanics underlying the problem under consideration. It is worth mentioning again that a very wide range of analysis types and complex geometries (curved, tapered) were dealt with, as well large displacements and elastoplastic materials.

Acknowledgments

The first author gratefully acknowledges the financial support of FCT (Fundação para a Ciência e a Tecnologia, Portugal), through the doctoral scholarship SFRH/BD/130515/2017.

References

- Bathe, K.J. (1996). *Finite Element Procedures* (1st ed.), Prentice-Hall Inc., New Jersey, USA.
- Bathe, K.J., Dvorkin, E.N. (1985). “A four-node plate bending element based on Mindlin/Reissner plate theory and a mixed interpolation.” *International Journal for Numerical Methods in Engineering*, Wiley, 21 (2) 367-383.

- Bebiano R., Gonçalves R., Camotim D. (2015). A cross-section analysis procedure to rationalise and automate the performance of GBT-based structural analyses, *Thin-Walled Structures*, **92**(July), 29-47.
- Bebiano R., Camotim D., Gonçalves R. (2018). GBTUL 2.0 – a second-generation code for the GBT-based buckling and vibration analysis of thin-walled members, *Thin-Walled Structures*, **124**(March), 235-257.
- Bianco, M., Habtemariam, A., Könke, C., Zabel, V. (2019). “Analysis of warping and distortion transmission in mixed shell-GBT (generalized beam theory) models.” *International Journal of Advanced Structural Engineering*, Springer, 11 109-126.
- Cai, J., Moen, C. (2016). “Elastic buckling analysis of thin-walled structural members with rectangular holes using Generalized Beam Theory.” *Thin-Walled Structures*, Elsevier, 107 274-286.
- Cai, J. (2019). “Obtaining the modal participation of displacements, stresses, and strain energy in shell finite-element eigen-buckling solutions of thin-walled structural members via generalized beam theory.” *Thin-Walled Structures*, Elsevier, 134 148-158.
- Camotim, D., Basaglia, C., Silvestre, N. (2010a). “GBT buckling analysis of thin-walled steel frames: a state-of-the-art report”, *Thin-Walled Structures*, Elsevier, 48 (10-11), 726-743.
- Camotim, D., Basaglia, C., Bebiano, R., Gonçalves, R., Silvestre, N. (2010b). “Latest developments in the GBT analysis of thin-walled steel structures”, *Proceedings of International Colloquium on Stability and Ductility of Steel Structures* (SDSS’Rio 2010 – 8-10/9), E. Batista, P. Vellasco, L. Lima (eds.), 33-58 (vol. 1).
- Camotim, D., Basaglia C., Silva N.F., Silvestre, N. (2010c). “Numerical analysis of thin-walled structures using Generalised Beam Theory (GBT): recent and future developments”, *Computational Technology Reviews*, Volume 1, B. Topping et al. (eds.), Saxe-Coburg Publications, Stirlingshire, 315-354.
- Camotim, D., Gonçalves, R., Basaglia, C. (2022). “Developments on the GBT-based stability analysis of thin-walled members and structural systems”, *Analysis and Design of Plated Structures – Volume 1: Stability* (2nd edition) N.E. Shanmugam, C.M. Wang (eds.), Woodhead Publishing (Series in Civil and Structural Engineering), Amsterdam, 133-175.
- Chroscielewski, J., Makowski, J., Stumpf, H. (1992). “Genuinely resultant shell finite elements accounting for geometric and material non-linearity.” *International Journal for Numerical Methods in Engineering*, Wiley, 35 (1) 63-94.
- Duan, L., Zhao, J. (2019). “GBT deformation modes for thin-walled cross-sections with circular rounded corners.” *Thin-Walled Structures*, Elsevier, 136 64-89.
- Eberlein, R., Wriggers, P. (1999). “Finite element concepts for finite elastoplastic strains and isotropic stress response in shells: theoretical and computational analysis.” *Computer Methods in Applied Mechanics and Engineering*, Elsevier, 171 (3) 243-279.
- Garcea, G., Gonçalves, R., Bilotta, A., Manta, D., Bebiano, R., Leonetti, L., Magisano, D., Camotim, D. (2016). “Deformation modes of thin-walled members: A comparison between the method of Generalized Eigenvectors and Generalized Beam Theory.” *Thin-Walled Structures*, Elsevier, 100 192-212.
- Gonçalves, R., Camotim, D. (2004). “GBT local and global buckling analysis of aluminium and stainless steel columns.”, *Computers & Structures*, Elsevier, 82 (17-19) 1473-1484.
- Gonçalves, R., Ritto-Corrêa, M., Camotim, D. (2010). “A large displacement and finite rotation thin-walled beam formulation including cross-section deformation.” *Computer Methods in Applied Mechanics and Engineering*, Elsevier, 199 (23-24) 1627-1643.
- Gonçalves, R., Ritto-Corrêa, M., Camotim, D. (2011). “Incorporation of wall finite relative rotations in a geometrically exact thin-walled beam element.” *Computational Mechanics*, Springer, 48 (2) 229-244.
- Gonçalves, R., Camotim, D. (2011). “Generalized Beam Theory-based finite elements for elastoplastic thin-walled metal members.” *Thin-Walled Structures*, Elsevier, 49 (10) 1237-1245.
- Gonçalves, R., Camotim, D. (2012). “Geometrically non-linear Generalized Beam Theory for elastoplastic thin-walled metal members.” *Thin-Walled Structures*, Elsevier, 51 121-129.
- Gonçalves, R., Camotim, D. (2017). “Improving the efficiency of GBT displacement-based finite elements.” *Thin-Walled Structures*, Elsevier, 111 165-175.
- Gonçalves R., Bebiano R., Camotim D. (2014). On the shear deformation modes in the framework of Generalised Beam Theory, *Thin-Walled Structures*, **84**(November), 325-334.
- Hansen, A., Jonsson, J. (2019). “Modelling of steel frames using advanced beam and joint elements with interfaces governed by beam modes.” *Thin-Walled Structures*, Elsevier, 145 106430 (14 pages).
- Hansen, A., Jonsson, J., Vieira, R. (2022). “Joint modelling in advanced thin-walled beam models.” *Thin-Walled Structures*, Elsevier, 171 108798 (22 pages).
- Henriques, D., Gonçalves, R., Camotim, D. (2015). “A physically non-linear GBT-based finite element for steel and steel-concrete beams including shear lag effects.” *Thin-Walled Structures*, Elsevier, 90 202-215.

- Henriques, D., Gonçalves, R., Camotim, D. (2016). GBT-based finite element to assess the buckling behaviour of steel-concrete composite beams." *Thin-Walled Structures*, Elsevier, 107 207-220.
- Manta, D., Gonçalves, R., Camotim, D. (2020). "Combining shell and GBT-based finite elements: linear and bifurcation analysis." *Thin-Walled Structures*, Elsevier, 152 paper 106665 (14 pages).
- Manta, D., Gonçalves, R., Camotim, D. (2021a). "Combining shell and GBT-based finite elements: plastic analysis with adaptive mesh refinement." *Thin-Walled Structures*, Elsevier, 158 paper 107205 (12 pages).
- Manta, D., Gonçalves, R., Camotim, D. (2021b). "Combining shell and GBT-based finite elements: Vibration and dynamic analyses." *Thin-Walled Structures*, Elsevier, 167 paper 108187 (11 pages).
- Manta, D., Gonçalves, R., Camotim, D. (2021c). "On the combination of shell and GBT-based beam finite elements." *Proceedings of the SSRC 2021 Annual Stability Conference*, virtual conference, USA (25 pages).
- MATLAB (2010), version 7.10.0 (R2010a), The MathWorks Inc., Massachusetts.
- de Miranda, S., Madeo, A., Melchionda, D., Ubertini, F. (2015). "A high performance flexibility-based GBT finite element." *Computers and Structures*, Elsevier, 158 285-307.
- Muresan, A.-A., Nedelcu, M., Gonçalves, R. (2019). "GBT-based FE formulation to analyse the buckling behaviour of isotropic conical shells with circular cross-section." *Thin-Walled Structures*, Elsevier, 134 84-101.
- Nedelcu, M. (2010). "GBT formulation to analyse the behaviour of thin-walled members with variable cross-section." *Thin-Walled Structures*, Elsevier, 48 (8) 629-638.
- Nedelcu, M. (2012). "GBT-based buckling mode decomposition from finite element analysis of thin-walled members." *Thin-Walled Structures*, 54 156-163.
- Peres N., Gonçalves R., Camotim D. (2021). "A geometrically exact beam finite element for curved thin-walled bars with deformable cross-section." *Computer Methods in Applied Mechanics and Engineering*, Elsevier, 381 113804 (30 pages).
- Reissner, E. (1972). "On one-dimensional finite-strain beam theory: the plane problem." *Journal of Applied Mathematics and Physics (ZAMP)*, Springer, 23 795-804.
- Ritto-Corrêa, M., Camotim, D. (2002). "On the differentiation of the Rodrigues formula and its significance for the vector-like parameterization of Reissner-Simo beam theory." *International Journal for Numerical Methods in Engineering*, Wiley, 55 (9) 1005-1032.
- Schardt, R. (1996). "Eine Erweiterung der Technischen Biegetheorie zur Berechnung prismatischer Faltwerke." *Stahlbau*, 35 (6) 161-171.
- Schardt, R. (1989). *Verallgemeinerte Technische Biegetheorie*, Springer Verlag, Berlin. (German)
- Simo, J. (1985). "A finite strain beam formulation. The three-dimensional dynamic problem, Part I." *Computer Methods in Applied Mechanics and Engineering*, Elsevier, 49 55-70.
- Simo, J., Taylor, R. (1985). "Consistent tangent operators for rate-independent elastoplasticity." *Computer Methods in Applied Mechanics and Engineering*, Elsevier, 48 (1) 101-118.